Void growth in ductile materials with actual porous microstructures

A. R. Vishnu, G. Vadillo, J. A. Rodríguez-Martínez*

Department of Continuum Mechanics and Structural Analysis. University Carlos III of Madrid. Avda. de la Universidad, 30. 28911 Leganés, Madrid, Spain

Abstract

In this paper, we have investigated void growth in ductile materials with actual porous microstructures. For that purpose, we have performed calculations of cubic unit-cells subjected to periodic boundary conditions and containing porosity distributions representative of three additively manufactured materials, namely, aluminium alloy AlSi10Mg, stainless steel 316L and Inconel 718. The initial void volume fraction in the calculations varies between 0.00564% and 1.75%, the number of voids between 14 and 5715, and the pores size from 2.3 μm to 110 μm. Several realizations with different void sizes and positions have been generated for each of the porous microstructures considered. The simulations have been carried out with random spatial distributions of voids and with clusters of different sizes. The matrix material is modeled using isotropic linear elasticity and von Mises plasticity with an associated flow rule and isotropic hardening, being the flow stress dependent on strain and strain rate. The macroscopic stress state in the unit-cell is controlled by prescribing constant triaxiality (T) and Lode parameter (L) throughout the loading. We have performed calculations with stress states resulting from a combination of three different triaxiality and Lode parameter values, i.e., $T = 1, 2, 3$ and $L = -1, 0, 1$. To the authors' knowledge, this is the first and the most comprehensive study that performs 3D unit-cell calculations with actual representation of porous microstructures, and analyzes the effects of size and spatial distribution of voids on the macroscopic response of the porous aggregate and on the collective behavior of individual pores. The results obtained with the actual porous microstructures have been compared with unit-cell calculations having an equivalent single central pore, and with calculations in which the material behaviour is modeled with Gurson plasticity. It has been shown that both initial void volume fraction and distribution of void sizes affect the macroscopic response of the porous aggregate and the void volume fraction evolution. Moreover, the calculations with random spatial distribution of voids have brought out that different realizations of the same microstructure carry significant variations to the effective behaviour of the porous aggregate, and that the interaction between neighboring pores dictates the volume evolution of individual voids, especially at higher macroscopic triaxiality. The calculations with clusters have shown that pores clustering promotes coalescence localization due to increased interaction between the voids, which results in an increased growth rate of voids in clusters with large number of pores.

*Corresponding author. E-mail address. jarmarti@ing.uc3m.es

Keywords:
Porous microstructure, Unit-cell calculations, Void growth, Coalescence, Clustering

1. Introduction

Ductile fracture in metals and alloys has been the subject of many studies over the past decades and it is known to (generally) occur by nucleation, growth (or closure) and coalescence of voids (Cox and Low, 1974; Benzerga and Leblond, 2010a; Benzerga et al., 2016; Pineau et al., 2016). Nucleation of voids usually starts at large inclusions and second-phase particles, by particle cracking or by decohesion of the particle–matrix interface. Void growth largely depends on the stress state, such that at low triaxiality voids tend to compress and collapse to ultimately form micro-cracks, and at high triaxiality they grow rapidly by diffuse plastic deformation of the surrounding matrix. When void growth is substantial, void coalescence occurs. The most common void coalescence mode is by internal necking of the intervoid ligament, i.e., the collapse of the ligaments between adjacent voids along a localization band perpendicular to the main loading direction that involves the formation of regions of elastic unloading separated from regions of highly localized plastic flow (the ligaments). Void growth induced softening may also initiate failure without void coalescence per se (Tekoğlu et al., 2015; Reboul et al., 2020).

The development of many existing ductile fracture models was motivated by the analysis of void growth in a plastic matrix. Notable are the pioneering studies of McClintock (1968), Rice and Tracey (1969), Hancock and Mackenzie (1976) and Gurson (1975, 1977), who described the growth of an isolated cylindrical or spherical void in an infinite rigid plastic solid. In particular, using micromechanical considerations, Gurson (1975, 1977) developed one of the most widely used criteria for porous solids containing spherical (or cylindrical) voids. The derivation of the Gurson (1975, 1977) model was based on a limit-analysis of a hollow sphere (or cylinder) of finite radius surrounded by the matrix material described with von Mises (1928) criterion and subjected to homogeneous boundary strain rate. Due to its intrinsic limitations to spherical or cylindrical voids and plastically isotropic materials, several extensions of the Gurson (1975, 1977) model have been proposed in various directions during the last decades to account for void nucleation (Chu and Needleman, 1980), void coalescence (Tvergaard and Needleman, 1984), void shape effects (Thomason, 1985; Gologanu et al., 1997; Jackiewicz, 2011), void size effects (Wen et al., 2005; Monchiet and Bonnet, 2013), void orientation (Danas and Ponte-Castañeda, 2009; Danas and Aravas, 2012) and distinct features of the constitutive model of the matrix material such as strain hardening (Leblond et al., 1995), viscoplasticity (Duva, 1986; Gărăjeu et al., 2000), plastic anisotropy (Benzerga and Besson, 2001; Benzerga et al., 2004; Chen and Dong, 2009) or pressure sensitivity (Cheng and Guo, 2007; Guo et al.,

2008; Thoré et al., 2009). Few attempts have been also made to include the Lode angle in the Gurson (1975, 1977) model to analyze the role of the third stress invariant in the ductile fracture of the porous material (Xue, 2008; Nahshon and Hutchinson, 2008; Benallal et al., 2014; Leblond and Morin, 2014; Vadillo et al., 2016). All the studies cited in this paragraph are based on the micromechanical analysis of a single void embedded in a plastic material. However, the presence of a non-uniform distribution of voids breaks the symmetry within the surrounding matrix and suggests the possibility of a void interaction effect. In a real material, the effect of void distribution observed from X-ray tomography experiments either for random (Maire and Withers, 2014) or clustered voids (Hannard et al., 2017) has been recognized to have an important contribution to ductile fracture.

Finite element unit-cell computations have been extensively used to provide fundamental understanding of the mechanical response of porous aggregates. Since the pioneering works of Needleman (1972) and Tvergaard (1981), a large number of unit-cell analyses has been conducted taking into account different cell configurations and loading conditions (Faleskog et al., 2000; Pardoen and Hutchinson, 2003; Kim et al., 2004a; Danas and Ponte-Castañeda, 2012; Keralavarma and Benzerga, 2010; Dæhli et al., 2018; Hosseini et al., 2022; Tekoğlu and Koçhan, 2022). In the original unit-cell framework, a single void is explicitly modeled and embedded in a matrix material with prescribed periodic boundary conditions. Nevertheless, this configuration does not provide information about microstructural features such as void evolution and interaction in a porous aggregate with non-periodic distribution of voids. In order to overcome this limitation, different works have extended the original unit-cell approach by modeling unit-cells embedding multiple voids. For instance, Thomson et al. (1998, 2003) performed finite element simulations of 3D unit-cells where few (three, four or eight) spherical pores were aligned with different orientations with respect to the loading directions. The orientation of the void distribution was shown to be a very important factor for void evolution and fracture. McVeigh et al. (2007) modeled the nucleation, growth and coalescence of several interacting pores in 2D and 3D unit-cells. Void spacing and relative void position were found to play an important role in void-sheet localization for zero stress triaxiality (shear loading). Tvergaard (2016, 2017) compared the behavior of several non-periodic distributions of pores embedded in representative volume elements against the behavior of a single pore with equal void volume fraction, and showed that faster void growth occurs for certain non-periodic void arrangements as compared to the single void case. Khan and Bhasin (2017) carried out three-dimensional finite element studies modeling explicitly both primary and secondary voids (i.e., larger and smaller voids). The ductile behavior of the porous aggregate was observed to significantly depend on the respective position of primary and secondary voids. Trejo Navas et al. (2018) carried out 3D finite element simulations of a material with a small population of voids and showed that for the same applied far-field stress, the growth of a void highly depends

on its relative position in the cell. Shakoor et al. (2018) assessed the competition between particle fragmentation and particle debonding and analyzed their respective influence on void coalescence considering a 3D unit-cell with a realistic population of particles (33 particles) obtained from X-ray tomography data. Recently, Hure (2021) and Cadet et al. (2021, 2022) simulated void growth and coalescence of random distributions of voids (initially spherical and identical in size) embedded in a cubic 3D cell. Specifically, Hure (2021) determined numerically the yield surfaces of porous isotropic materials containing random spatial distributions of voids. The comparison of 3D unit-cells with different number of voids (up to 64), showed that the maximum stress in the simulations –which was used to compute the numerical yield surfaces– is less dependent on the porosity distribution as the number of voids increases. The numerical yield surfaces were found to be consistent with a multi-surface yield criterion accounting for both homogeneous and inhomogeneous material yielding. Moreover, the coalescence process was found to be substantially affected by the distribution of voids, such that the coalescence strain was smaller for the material with random spatial distribution of voids as compared to calculations performed with periodic porous microstructures. Cadet et al. (2021) investigated plastic strain localization in 3D cubic cells made of an elastic-perfectly plastic matrix with random spatial distribution of identical non-overlapping spherical voids (number of voids equal to 27). Various proportional loading conditions with controlled stress triaxiality and Lode parameter were applied (up to the final fracture of the cell), with the microstructures with random spatial distribution of voids showing earlier coalescence as compared to unit-cells with a single central void (and the same void volume fraction). The random distribution of voids led to a large variability of failure strains due to inhomogeneous plastic strain field induced by the porous microstructure. The work of Cadet et al. (2021) was extended shortly after by Cadet et al. (2022) to consider loading cases in which the principal axes of the applied stress are systematically varied with respect to the unit-cell axes. The minimum fracture strain of the porous aggregate was found to draw a U-shape curve function of the Lode parameter (L), with a minimum value near $L = 0$ (generalized shear stress).

Finite element simulations including distributions of voids obtained from X-ray tomography analysis of porous materials bring about opportunities to study ductile damage in more realistic situations. The idea is to elucidate the role of real void sizes or real intervoid distances on the mechanisms of ductile fracture. However, to the authors' knowledge, an experimentally-based void configuration with a number of pores large enough to ensure a significant statistical representation of the porous microstructure was never fully mapped within a 3D representative volume element. This is precisely the gap we intend to fill in this paper. For that purpose, we have developed a microstructurally-informed finite element unit-cell model to determine the role of actual porosity on the macroscopic response of the porous aggregate. The cubic unit-cell is subjected to different loading conditions characterized by prescribed (constant) stress triaxiality

and Lode parameter. We have created porous microstructures with random spatial distributions of voids based on the X-ray tomography measurements reported by Marvi-Mashhadi et al. (2021) for 3 different additively manufactured materials, namely, aluminium alloy AlSi10Mg, stainless steel 316L and Inconel 718. The pores are taken to be initially spherical, consistent with the X-ray tomography measurements and the SEM micrographs reported by Nieto-Fuentes et al. (2022a). Several realizations have been generated for each of the porous microstructures considered and the results have been compared with unit-cells with a single central pore, and with calculations in which the material is modeled using Gurson plasticity. The main novelty of this research as compared to recently published papers is: (1) considering larger (and real) population of spherical voids to ensure that the numerical results are statistically significant and (2) including experimentally-measured distributions of void sizes. The calculations provide new insights into the effects of size and spatial distribution of voids on the macroscopic response of the porous material and allow for characterization of the collective behavior and interaction of individual pores.

The paper is organized as follows. Section 2 shows the elasto-plastic constitutive framework used to define the mechanical behavior of the material. Section 3 describes the unit-cell finite element model and the main features of the porous microstructures investigated. The effect of stress triaxiality and Lode parameter on the effective behavior of the unit-cell, on the evolution of the void volume fraction and on the growth of individual voids is analyzed in Section 4. A parametric study on the influence of initial void volume fraction and distribution of void sizes on the mechanical behavior of the porous aggregate is performed in Section 5, including comparisons with results obtained with unit-cells containing a single central pore, and with unit-cells modeled using Gurson plasticity. Section 6 shows calculations with clustering microstructures having the same initial void volume fraction and different number of clusters of different sizes. A summary of the main findings of the paper is given in Section 7.

2. Constitutive framework

The mechanical behavior of the material is assumed to follow isotropic linear elasticity and von Mises (1928) plasticity. The total rate of deformation tensor $\boldsymbol{d}$ is decomposed into elastic ($\boldsymbol{d}^e$) and plastic ($\boldsymbol{d}^p$) components:

$$\boldsymbol{d} = \boldsymbol{d}^e + \boldsymbol{d}^p \tag{1}$$

The elastic deformation rate is related to the rate of the stress:

$$\dot{\boldsymbol{\sigma}} = \boldsymbol{C} : \boldsymbol{d}^e \tag{2}$$

where $\dot{\boldsymbol{\sigma}}$ is an objective derivative of the Cauchy stress tensor and $\boldsymbol{C} = 2G\tilde{\mathbf{I}} + K\mathbf{1} \otimes \mathbf{1}$ is the tensor of isotropic elastic moduli, with G being the elastic shear modulus, K the bulk modulus, $\mathbf{1}$ the second-order unit tensor and $\tilde{\mathbf{I}}$ the fourth-order deviatoric unit tensor.

The plastic deformation rate follows an associated flow rule:

$$\boldsymbol{d}^p = \dot{\lambda}\frac{\partial f}{\partial \boldsymbol{\sigma}} \tag{3}$$

where $\dot{\lambda}$ is the plastic flow proportionality factor and $f = \bar{\sigma} - \sigma_Y \leq 0$ is the yield condition, with $\bar{\sigma} = \sqrt{\frac{3}{2}\boldsymbol{s} : \boldsymbol{s}}$ being the von Mises effective stress, where $\boldsymbol{s} = \boldsymbol{\sigma} - \sigma_h : \mathbf{1}$ and $\sigma_h = \frac{1}{3}\boldsymbol{\sigma} : \mathbf{1}$. Moreover, σ_Y is the yield stress of the material which is assumed to be a function of the effective plastic strain ($\bar{\epsilon}^p$) and the effective plastic strain rate ($\dot{\bar{\epsilon}}^p$):

$$\sigma_Y(\bar{\epsilon}^p, \dot{\bar{\epsilon}}^p) = \sigma_0(\bar{\epsilon}^p + \epsilon_0)^n \left(\frac{\dot{\bar{\epsilon}}^p}{\dot{\epsilon}_0}\right)^m \tag{4}$$

where $\bar{\epsilon}^p = \int_0^t \dot{\bar{\epsilon}}^p(\tau)d\tau$ and $\dot{\bar{\epsilon}}^p = \sqrt{\frac{2}{3}\,\boldsymbol{d}^p : \boldsymbol{d}^p}$. The parameter σ_0 is the initial yield stress, and n and m are the strain hardening and strain rate sensitivity exponents, respectively. Moreover, ϵ_0 and $\dot{\epsilon}_0$ are the reference strain and strain rate.

The baseline numerical values used in the finite element simulations of Sections 4, 5 and 6 for the initial density, the elastic constants and the parameters of the yield stress correspond to aluminum alloy 2090-T3 (Yoon et al., 2006; Cvitanić et al., 2008). Moreover, additional calculations with parameters corresponding to aluminum alloys 6111-T4 and 6013 are included in Appendix A to illustrate the effect of material behavior on the evolution of the porous microstructure. While these three materials display plastic anisotropy (Barlat et al., 2005; Kim et al., 2010; Ha et al., 2018), all the finite element simulations in this paper are carried out using isotropic von Mises plasticity to facilitate the interpretation of results. The effect of plastic anisotropy on the evolution of the porous microstructure will be studied in a future work.

Symbol	Property and units	Aluminium alloy 2090-T3
ρ_0	Initial density (kg/m^3)	2700
G	Elastic shear modulus (GPa)	26.92
K	Bulk modulus (GPa)	58.33
σ_0	Initial yield stress parameter (MPa), Eq. (4)	646
n	Strain hardening exponent, Eq. (4)	0.227
m	Strain rate sensitivity exponent, Eq. (4)	0.01
ϵ_0	Reference strain, Eq. (4)	0.025
$\dot{\epsilon}_0$	Reference strain rate (s^{-1}), Eq. (4)	0.0001

Table 1: Numerical values of initial density, elastic constants and parameters of the yield stress corresponding to aluminum alloy 2090-T3 (Yoon et al., 2006; Cvitanić et al., 2008).

3. Finite element model

The finite element model is a cubic unit-cell containing spatially distributed spherical voids of different sizes, which is considered to be a representative volume element of a porous material, see Fig. 1. The equations for the nodal displacements reported in Appendix A of Dakshinamurthy et al. (2021) have been used to impose periodic boundary conditions on the unit-cell, so that the displacement of opposed external nodes is coupled (i.e., the displacement of the nodes in the outer faces of the unit-cell is coupled). Material points are referred to using a 3D Cartesian coordinate system (x,y,z) with origin located at the bottom right corner of the cell, see Fig. 1. The loading directions are determined by the axes x, y and z (see below). Note that the contour plots in Figs. 3, 18, 23 and 27 are referred to this coordinate system. The initial configuration of the unit-cell is defined by the domain $0 \leq x \leq L_0$, $0 \leq y \leq L_0$, and $0 \leq z \leq L_0$, with $L_0 = 1$ mm.

The macroscopic stress tensor is taken as the volumetric averaging of the microscopic (local) Cauchy stress tensor (Vadillo et al., 2016; Hosseini et al., 2022):

$$\boldsymbol{\Sigma} = \frac{1}{V^{cell}} \int_{V^{cell}} \boldsymbol{\sigma} dV^{cell} \tag{5}$$

where V^{cell} is the total volume of the unit-cell.

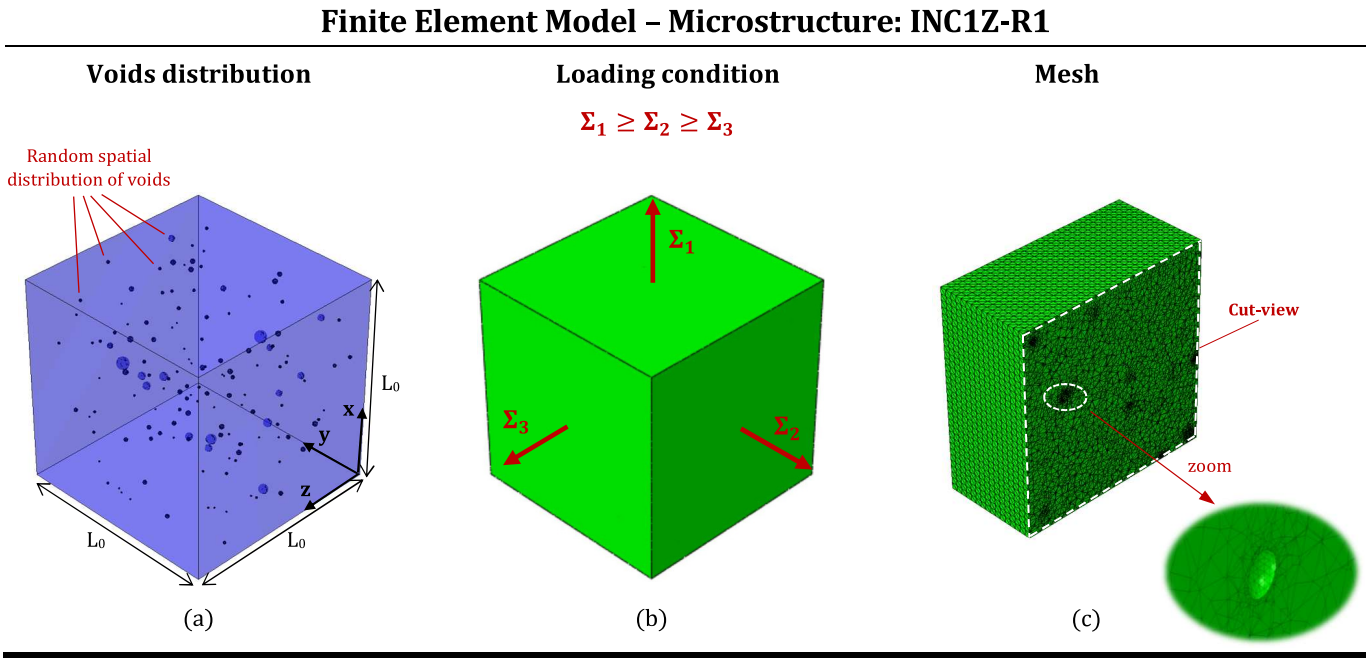

Figure 1: Unit-cell finite element model: (a) semi-transparent view displaying the porous microstructure, (b) loading conditions with Σ_1, Σ_2 and Σ_3 being the principal values of the macroscopic stress tensor and (c) cut-view showing the fine mesh around the voids.

The macroscopic strain tensor is defined as the volumetric averaging of the microscopic (local) logarithmic strain tensor (Dakshinamurthy et al., 2021; Hosseini et al., 2022):

$$\boldsymbol{\varepsilon} = \frac{1}{V^{matrix}} \int_{V^{matrix}} \boldsymbol{\epsilon} dV^{matrix} \tag{6}$$

where $V^{matrix} = V^{cell} - V^{voids}$ is the volume of the matrix material, with V^{voids} being the volume of all the voids included in the unit-cell.

The multi-point constraint subroutine developed by Dakshinamurthy et al. (2021) has been used to enforce constant and controlled values of the macroscopic stress triaxiality $T = \frac{\Sigma_h}{\overline{\Sigma}}$ and the macroscopic Lode parameter $L = \frac{2\Sigma_2 - \Sigma_1 - \Sigma_3}{\Sigma_1 - \Sigma_3}$ during the calculations, where $\Sigma_h = \frac{\Sigma_1 + \Sigma_2 + \Sigma_3}{3}$ and $\overline{\Sigma} = \sqrt{\frac{3}{2}\boldsymbol{\Sigma}' : \boldsymbol{\Sigma}'}$ are the macroscopic hydrostatic stress and the macroscopic effective stress, respectively, and Σ_1, Σ_2 and Σ_3 ($\Sigma_1 \geq \Sigma_2 \geq \Sigma_3$) are the principal values of the macroscopic stress tensor, with $\boldsymbol{\Sigma}' = \boldsymbol{\Sigma} - \Sigma_h \mathbf{1}$. The loading directions are aligned with the principal directions of the macroscopic stress tensor, so that the major loading direction corresponds to the principal stress direction associated to Σ_1 (parallel to x), and the minor loading direction corresponds to the principal stress direction associated to Σ_3 (parallel to z), see Fig. 1. Moreover, the macroscopic effective strain is $\overline{\varepsilon} = \sqrt{\frac{2}{3}\boldsymbol{\varepsilon}' : \boldsymbol{\varepsilon}'}$, where $\boldsymbol{\varepsilon}' = \boldsymbol{\varepsilon} - \varepsilon_h \mathbf{1}$ and $\varepsilon_h = \frac{\varepsilon_1 + \varepsilon_2 + \varepsilon_3}{3}$, with ε_1, ε_2

and ε_3 ($\varepsilon_1 \geq \varepsilon_2 \geq \varepsilon_3$) being the principal values of the macroscopic strain tensor. Note that the tensors $\boldsymbol{\Sigma}$ and $\boldsymbol{\varepsilon}$ do not determine the stress and strain states in a material point, but they are rather used for the definition of the macroscopic stress and strain scalars required for the graphical representation and interpretation of results.

The novelty of the numerical simulations is that we have incorporated into the unit-cell calculations the porous microstructure obtained from three additively manufactured metals –aluminium alloy AlSi10Mg (Al3XY), stainless steel 316L (SS5XY) and Inconel 718 (INC1Z)– following the methodology developed by Marvi-Mashhadi et al. (2021) and later adopted by Vishnu et al. (2022a,b) and Nieto-Fuentes et al. (2022b) to study the effect of actual porosity on the formation of necks and shear bands at high loading rates (i.e., so far, the methodology has been used to address problems other than void growth in unit-cell calculations under controlled triaxiality and Lode parameter). Recall that the pores are taken to be spherical, consistent with the X-ray tomography measurements and the SEM micrographs reported by Nieto-Fuentes et al. (2022a) for AlSi10Mg specimens. Intersections between voids, and between voids and unit-cell boundaries are not allowed. We have created porous microstructures with random spatial distribution of voids and with void clusters.

The main features of the porous microstructures investigated, which are obtained from the X-ray tomography measurements of Marvi-Mashhadi et al. (2021), are reported in Table 2: initial void volume fraction (f_0), number of voids per mm^3 (N_v), maximum voids diameter (d_{max}), minimum voids diameter (d_{min}), and mean (μ) and standard deviation (dev) of fitted Log-normal distribution.

For each of the three porous microstructures considered, for the microstructures with random spatial distribution of voids, we have generated up to five realizations of void size and position distribution which meet the same Log-normal statistical function. The goal is to take into account the scatter in the finite element results caused by the random spatial distribution of pores, see Section 4 for details. These realizations will be referred to as R1, R2, ... , R5. The initial void volume fraction (f_0), the number of voids (N_t), and the maximum void diameter (d_{max}) in the unit-cell calculations of the realizations created for each of the microtructures investigated are shown in Table 3. The difference in the void volume fraction between the experimental measurements and the computations –compare Tables 2 and 3– is partially caused by the random nature of the position of the voids and of the distribution of void sizes in the experimental specimen (see Marvi-Mashhadi et al. (2021)), which is carried over to the finite element model, leading to deviations from the number of pores measured in the tomograms (which are taken over a greater volume, see Marvi-Mashhadi et al. (2021)). Note also that the void volume fraction in the finite element models is less than the experimental data reported in Table 2 because the intersections between voids, and between voids and specimen boundaries are not allowed (as mentioned

before), so that several pores are eventually removed from the finite element models.

Moreover, separate attention has been paid to the effect of pore clustering on the evolution of the macroscopic response of the unit-cell and the void volume fraction. For the microstructures with clusters, the methodology developed by Graham-Brady (2010) has been adapted to generate finite element models based on the microstructures of Table 2 with different number of void clusters, see Section 6 for details.

	Al3XY	SS5XY	INC1Z
f_0 (%)	2.17	0.0025	0.1363
N_v (num./mm^3)	5985	17	147
d_{max} (μm)	110.53	41.40	78.93
d_{min} (μm)	8.00	7.40	7.45
μ (μm)	15.98	11.21	16.58
dev (μm)	4.57	5.13	7.71

Table 2: Summary of the porous microstructures investigated in this work: initial void volume fraction (f_0), number of voids per mm^3 (N_v), maximum diameter of voids (d_{max}), minimum diameter of voids (d_{min}), and mean (μ) and standard deviation (dev) values of fitted Log-normal distribution. Experimental measurements of Marvi-Mashhadi et al. (2021).

	Al3XY			SS5XY			INC1Z				
	R1	R2	R3	R1	R2	R3	R1	R2	R3	R4	R5
f_0 (%)	1.75	1.62	1.60	0.00663	0.00626	0.00564	0.0735	0.0416	0.0418	0.0666	0.0679
N_t (num.)	5715	5642	5647	15	17	17	143	143	138	141	144
d_{max} (μm)	86.77	91.33	86.88	30.34	31.28	37.56	58.91	60.29	36.16	52.83	64.67
d_{min} (μm)	7.4	7.4	7.4	7.4	7.4	7.4	7.4	7.4	7.4	7.4	7.4

Table 3: Initial void volume fraction (f_0), number of voids (N_t), maximum void diameter (d_{max}) and minimum void diameter (d_{min}) in the finite element models corresponding to the realizations generated for the microstructures with random spatial distribution of voids.

The finite element calculations have been performed using ABAQUS/Standard (2019). The unit-cell has been discretized with ten-node quadratic tetrahedral elements (C3D10 in ABAQUS notation). A very fine mesh near the pores is necessary to capture the geometry and the subsequent shape evolution of the voids during loading, see Fig. 1. The number of elements increases with the number of pores, so that ≈ 5000000, ≈ 200000 and ≈ 350000 elements are used to mesh the unit-cells corresponding to microstructures Al3XY, SS5XY and INC1Z, respectively. The calculations have been performed using a workstation AMD Milan 7453 @ 2.75 GHz with 56 cores. The computational cost of each simulation ranged between 2 and 12 days, depending on the microstructure considered, using simultaneously all the cores of the workstation.

The evolution of the void volume fraction (f) in the unit-cell during loading is calculated as:

$$f = \frac{V^{cell} - V^{matrix}}{V^{cell}} \tag{7}$$

where the volume of the matrix material is computed as:

$$V^{matrix} = \sum_{n=1}^{n_{elem}} EVOL_n \tag{8}$$

where $EVOL$ is the elemental volume and n_{elem} is the total number of elements in the model. We have also calculated the volume evolution of individual voids using the Quickhull algorithm (Barber et al., 1996) available in MATLAB® to compute the smallest convex set containing the nodal coordinates of the void surface at each time step.

Sections 4, 5 and 6 include calculations for three different values of macroscopic triaxiality $T = 1$, 2 and 3, and macroscopic Lode parameter $L = -1$, 0 and 1. Note that for $L = -1$ we have that $\Sigma_1 > \Sigma_2 = \Sigma_3$ (axisymmetric tension), for $L = 0$ the principal values of the macroscopic stress tensor are such that $\Sigma_1 > \Sigma_2 = \frac{\Sigma_1 + \Sigma_3}{2} > \Sigma_3$ (generalized shear), and for $L = 1$ we have that $\Sigma_1 = \Sigma_2 > \Sigma_3$ (axisymmetric compression).

4. Salient results

The calculations correspond to porous microstructure INC1Z and realizations R1, R2, ... , R5. The effect of microstructural realization, stress triaxiality and Lode parameter on the macroscopic effective behavior of the unit-cell, on the evolution of the normalized void volume fraction and on the growth of individual voids is investigated in Sections 4.1, 4.2 and 4.3, respectively.

4.1. The effect of microstructural realization

Fig. 2 compares calculations performed with realizations R1, R2, ... , R5 for stress triaxiality $T = 3$ and Lode parameter $L = -1$ (all the calculations in Section 4.1 are performed with $T = 3$ and $L = -1$). The evolution of the normalized macroscopic effective stress $\bar{\Sigma}/\sigma_0$ with the macroscopic effective strain $\bar{\varepsilon}$ is shown in Fig. 2a. The differences between realizations increase with the effective strain, e.g., the maximum effective stress is 5% larger for R2 than for

R1. The influence of the realization on the $\bar{\Sigma}/\sigma_0 - \bar{\varepsilon}$ curves comes from the differences in the void volume fraction between R1, R2, ... , R5, and also from the different spatial and size distribution of voids. Fig. 2b shows the evolution of the normalized void volume fraction f/f_0 with the macroscopic effective strain $\bar{\varepsilon}$. The $f/f_0 - \bar{\varepsilon}$ curves display a concave-upward shape, so that the porosity growth rate increases as the loading progresses (due to the large value of imposed triaxiality, e.g., see Hosseini et al. (2022)). Notice that the calculations which show greater porosity growth rate, R2, R3 and R5, are the same displaying faster strain softening in Fig. 2a. The key outcome of these results is that, despite all realizations correspond to the same porous microstructure, there are significant differences in the evolution of macroscopic stress and porosity, consistent with the scatter generally observed in mechanical characterization tests of additively manufactured materials (Kristoffersen et al., 2020).

Unit-cells showing contour plots of effective plastic strain in the matrix material $\bar{\epsilon}^p$ for realizations R1 and R3 are included in Fig. 3. The results correspond to different values of macroscopic effective strain $\bar{\varepsilon} = 0, 0.033, 0.066$ and 0.1, which are indicated in Fig. 2 with yellow markers. The color coding of the isocontours is such that effective plastic strains ranging from 0 to 1 correlate with a color scale that goes from blue to red. Effective plastic strains above 1 remain red. The semi-transparent view of the specimen in pictures (a)-(h) shows the evolution of the porous microstructure, and the solid cut-views in pictures (d) and (h) illustrate the localization of plastic deformation and the pores coalescence localization. There are no qualitative differences between the contours corresponding to R1 and R3. Semi-transparent pictures (a) and (e) show the unit-cells before loading starts. The microstructures contain pores of different sizes randomly distributed in the sample. For $\bar{\varepsilon} = 0.033$, see pictures (b) and (f), the pores have already significantly grown, and the effective plastic strain near the voids has reached values greater than 1. Notice the contrast between macroscopic strain and local plastic deformation near the voids, the latter being much greater (the relationship between macroscopic strain and local plastic deformation will be further discussed below). The contours in (c) and (g) for $\bar{\varepsilon} = 0.066$ correspond approximately to the maximum macroscopic effective stress, see Fig. 2a, and the void volume fraction is roughly ten times more than at the beginning of loading, see Fig. 2b. Notice that the localization of plastic deformation at specific locations of the outer faces of the unit-cell comes from the growth of nearby voids. Semi-transparent pictures (d) and (h) are taken for $\bar{\varepsilon} = 0.1$, during the strain softening process. The porosity for realizations R1 and R3 is nearly 30 and 40 times greater than initially, respectively. The cut-view pictures show cross-sections of voids of different sizes and illustrate the interaction between nearby pores that have grown, leading to large values of plastic deformation in the intervoid ligament. While fracture is not accounted for in the finite element calculations, coalescence of voids is apparent (see pinkish arrows), as they are just separated by very elongated necked sections. Tekoğlu et al. (2015) determined coalescence localization to

occur when all the additional plastic deformation is confined within the ligaments between the voids, consistent with the early modeling of coalescence of Thomason (1990) and subsequent researchers (Benzerga and Leblond, 2010b; Tekoğlu et al., 2012). Fig. 4 shows different contours of effective plastic strain in the surface of the two pores indicated in the cut-view of image 3(d), from the onset of loading until $\bar{\varepsilon} = 0.116$, for intervals of macroscopic strain of 0.016. The pores remain virtually spherical until $\bar{\varepsilon} = 0.05$ (for this large value of triaxiality $T = 3$, the voids which do not interact with nearby pores tend to grow maintaining the spherical shape). At this stage of the loading process, the entire surface of the voids shows effective plastic strains greater than 1. Note that the plastic strain surrounding the pores increased from 0.5 to more than 1 within a narrow interval of macroscopic strain ($0.016 \leq \bar{\varepsilon} \leq 0.05$) which is fifteen times less, i.e., the local plastic strain increases fifteen times faster than the macroscopic strain. For macroscopic strains greater than 0.066, the growth of the pores make them to interact and flatten, leading to the formation of a thin intervoid ligament subjected to large plastic strain which shows coalescence localization (coalescence would be completed by considering a fracture criterion in the simulations).

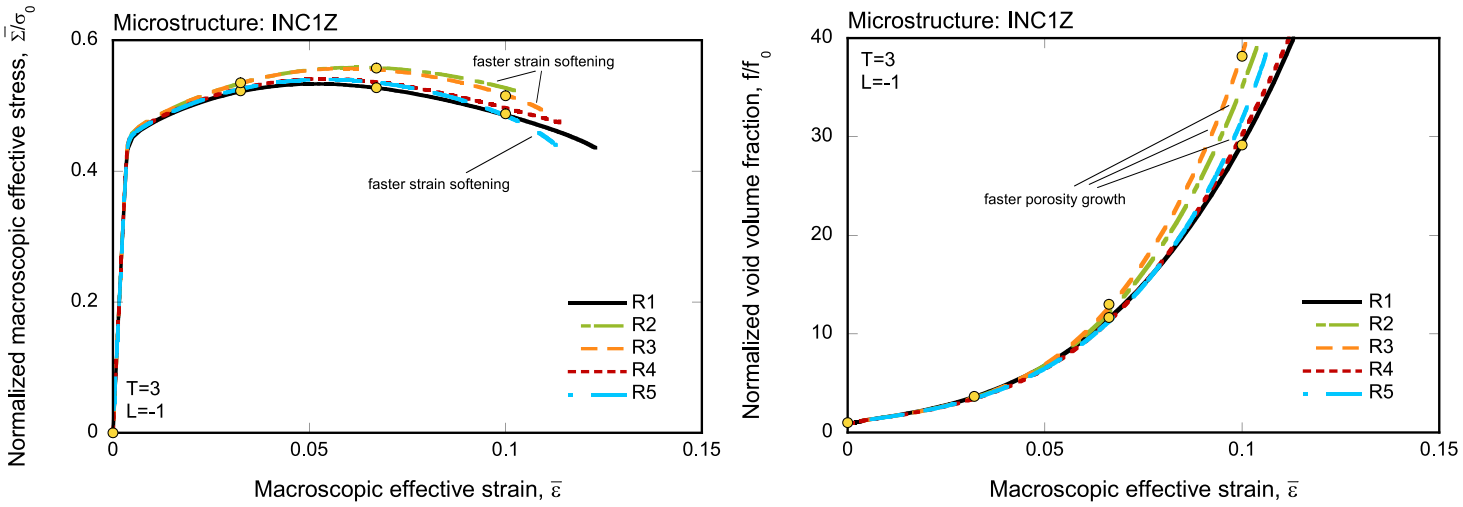

Figure 2: Results corresponding to porous microstructure INC1Z and realizations R1, R2, ... , R5 for stress triaxiality $T = 3$ and Lode parameter $L = -1$. (a) Normalized macroscopic effective stress $\bar{\Sigma}/\sigma_0$ versus macroscopic effective strain $\bar{\varepsilon}$. (b) Normalized void volume fraction f/f_0 versus macroscopic effective strain $\bar{\varepsilon}$. The yellow markers correspond to realizations R1 and R3, for different values of the macroscopic effective strain $\bar{\varepsilon} = 0, 0.033, 0.066$ and 0.1 shown in the contour plots of Fig. 3. (For interpretation of the references to color in this figure legend, the reader is referred to the web version of this article.)

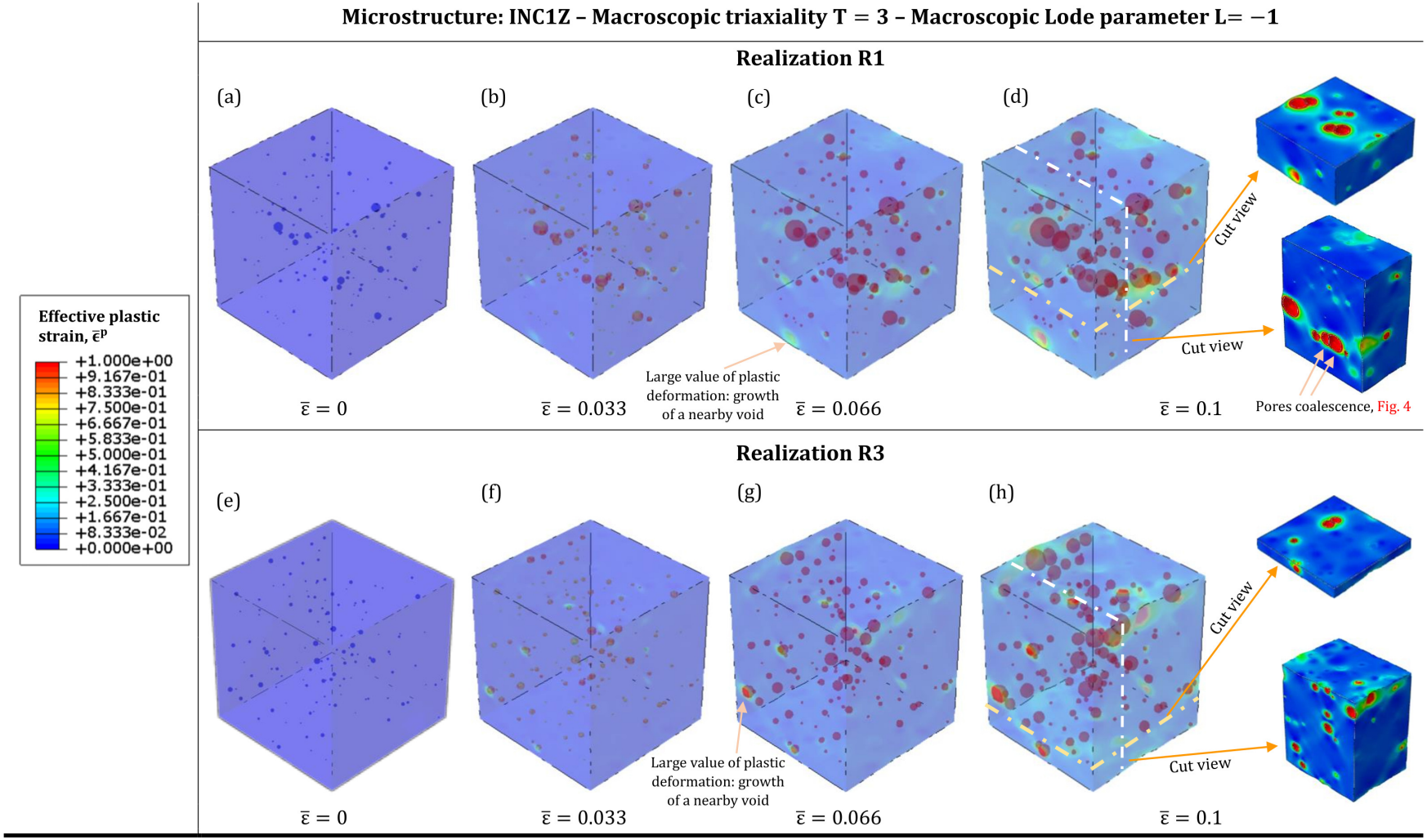

Figure 3: Results corresponding to porous microstructure INC1Z for stress triaxiality $T = 3$ and Lode parameter $L = -1$. Contours of effective plastic strain in the matrix material $\bar{\epsilon}^p$ for different values of macroscopic effective strain $\bar{\varepsilon} = 0, 0.033, 0.066$ and 0.1. (a)-(d) Realization R1. (e)-(h) Realization R3. (For interpretation of the references to color in this figure legend, the reader is referred to the web version of this article.)

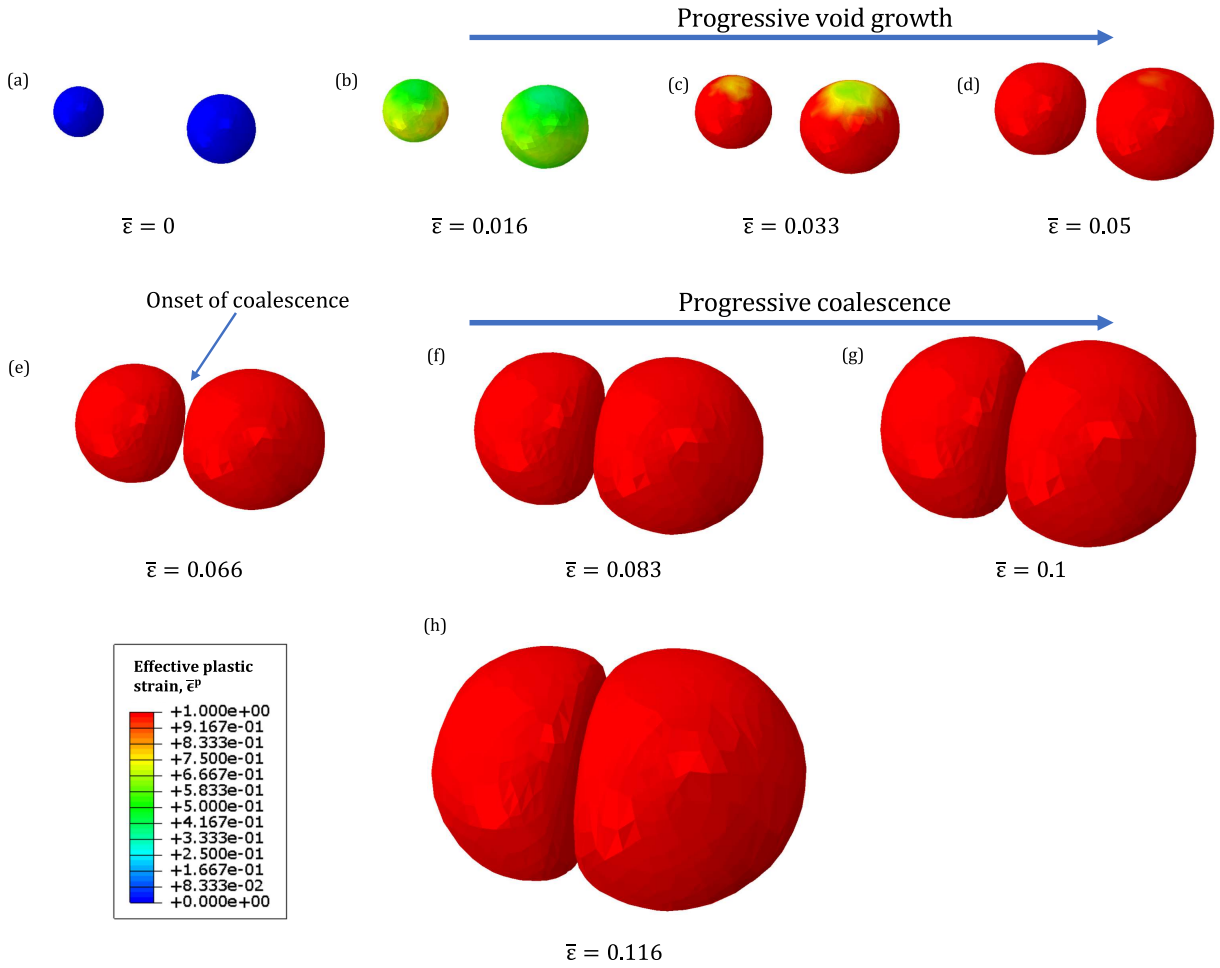

Figure 4: Results corresponding to porous microstructure INC1Z and realization R1 for stress triaxiality $T = 3$ and Lode parameter $L = -1$. Contours of effective plastic strain $\bar{\epsilon}^p$ in two neighboring pores indicated in Fig. 3(d) for different values of macroscopic effective strain: (a) $\bar{\varepsilon} = 0$, (b) $\bar{\varepsilon} = 0.016$, (c) $\bar{\varepsilon} = 0.033$, (d) $\bar{\varepsilon} = 0.05$, (e) $\bar{\varepsilon} = 0.066$, (f) $\bar{\varepsilon} = 0.083$, (g) $\bar{\varepsilon} = 0.1$ and (h) $\bar{\varepsilon} = 0.116$. (For interpretation of the references to color in this figure legend, the reader is referred to the web version of this article.)

The interaction between neighboring pores make that these grow at different rates depending on their spatial location in the unit-cell. Fig. 5 shows the normalized volume of individual pores $V^{\text{void}}/V_0^{\text{void}}$ versus the macroscopic effective strain $\bar{\varepsilon}$ for realization R1 (note that V^{void} and V_0^{void} are the current and initial volume of the voids, respectively). Fig. 5a includes the results for the five largest pores of the microstructure, which have diameters varying from 58.9 μm to 40.9 μm. There is no direct relationship between the size of the voids and their growth rate, as the pore growing faster is void 3 ($d = 45.1$ μm), followed by voids 1 and 5 ($d = 58.9$ μm and 40.9 μm, respectively). Note that for the pores displaying slower growth rate, voids 2 and 4, the $V^{\text{void}}/V_0^{\text{void}} - \bar{\varepsilon}$ curves do not show a concave-upward shape, but the increase of the volume of the void is roughly linear with the macroscopic strain. Fig. 5b shows results for five intermediate size voids and, similarly to Fig. 5a, the rate of growth of the pores does not find an explicit relationship

with their initial diameter. For instance, Figs. 6 and 7 include 3D reconstructions of the two pores with initial diameter 33.1 μm (voids 3 and 4 in Fig. 5b) showing that while having the same initial size, the growth of void 4 is much faster (the voids geometry has been reconstructed plotting the surface defined by the convex hull that forms the surface of the voids). In fact, void 4 is no longer spherical for large macroscopic strain, as it approaches coalescence (with another nearby pore of the microstructure, as in Fig. 4). Moreover, Fig. 5c shows the evolution of the volume of the five smallest pores of the microstructure, which all have initial diameter of 7.4 μm. Note that voids 2 and 4 grow much faster than voids 1, 3 and 5 for values of the macroscopic strain greater than 0.05, as the latter display a (quasi)linear growth during the whole loading process. Based on the results of Fig. 5, ~ 0.05 seems to be a critical value of the macroscopic strain which determines the beginning of the *accelerated* growth rate of the voids for $T = 3$ and $L = -1$ (this critical value depends on the loading path, as discussed in Section 4.2).

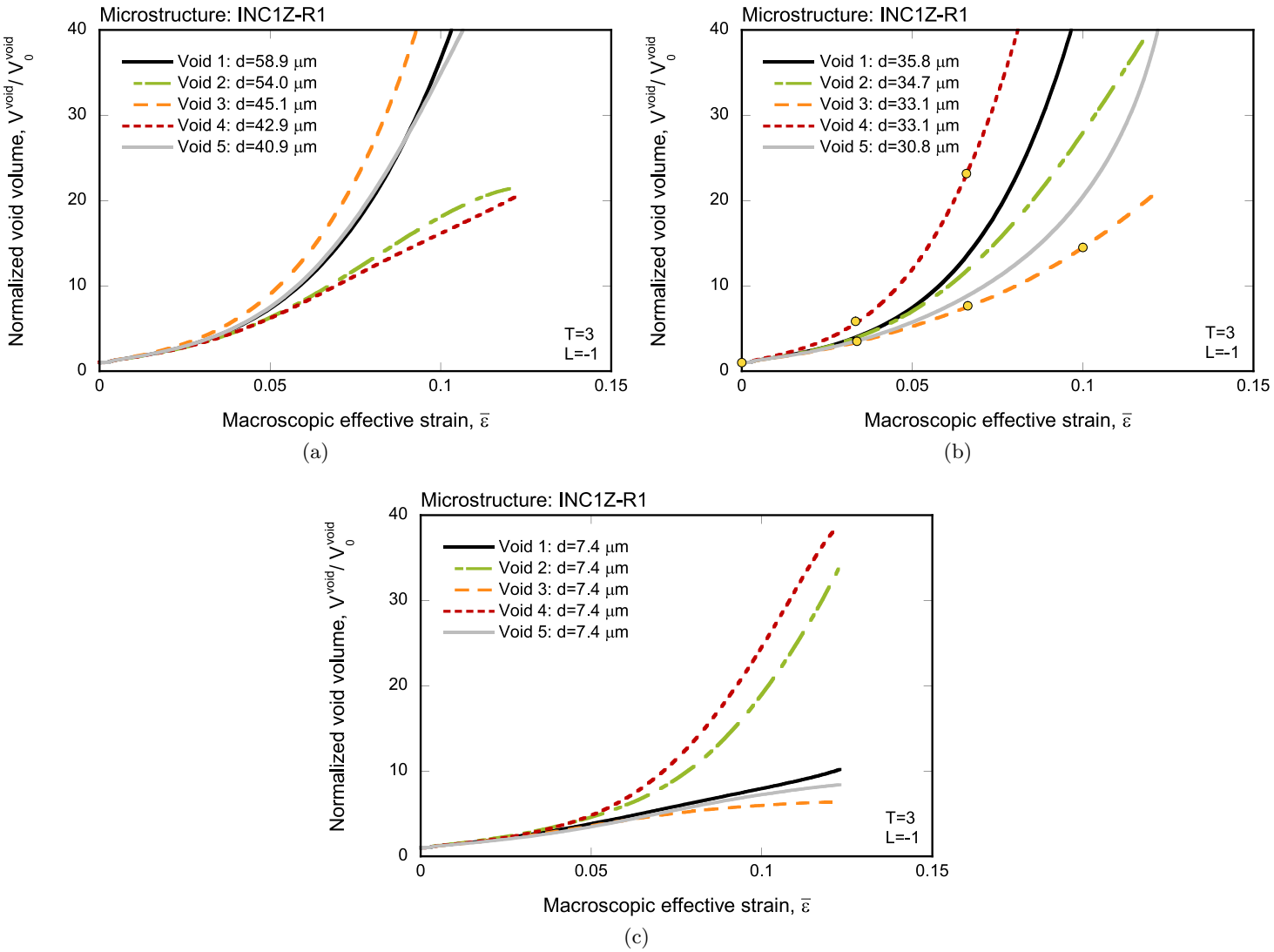

Figure 5: Results corresponding to porous microstructure INC1Z and realization R3 for stress triaxiality $T = 3$ and Lode parameter $L = -1$. Normalized void volume $V^{\text{void}}/V_0^{\text{void}}$ versus macroscopic effective strain $\bar{\varepsilon}$. (a) Largest pores of the microstructure with diameters varying from 58.9 μm to 40.9 μm, (b) intermediate pores of the microstructure with diameters varying from 35.8 μm to 30.8 μm and (c) smallest pores of the microstructure with diameter 7.4 μm. The yellow markers indicate different values of the macroscopic effective strain corresponding to the 3D reconstructions of voids 3 and 4 included in Figs. 6 and 7. (For interpretation of the references to color in this figure legend, the reader is referred to the web version of this article.)

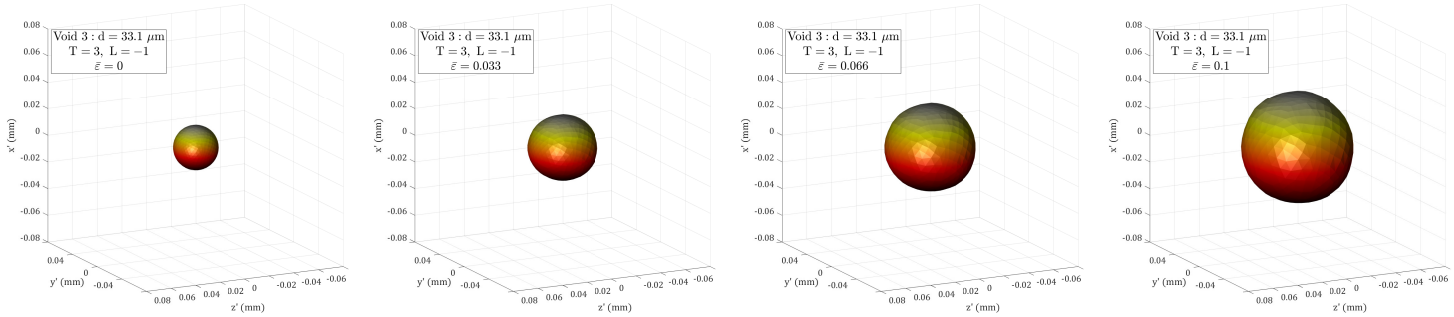

(a) (b) (c) (d)

Figure 6: Results corresponding to porous microstructure INC1Z and realization R1 for stress triaxiality $T = 3$ and Lode parameter $L = -1$. 3D reconstruction of the surface of void 3 included in Fig. 5b with initial diameter $d = 33.1$ μm for different values of the macroscopic effective strain: (a) $\bar{\varepsilon} = 0$, (b) $\bar{\varepsilon} = 0.033$, (c) $\bar{\varepsilon} = 0.066$ and (d) $\bar{\varepsilon} = 0.1$. The origin of the Cartesian coordinate system (x', y', z') is located at the center of mass of the void, with x', y' and z' being parallel to the loading axes x, y and z.

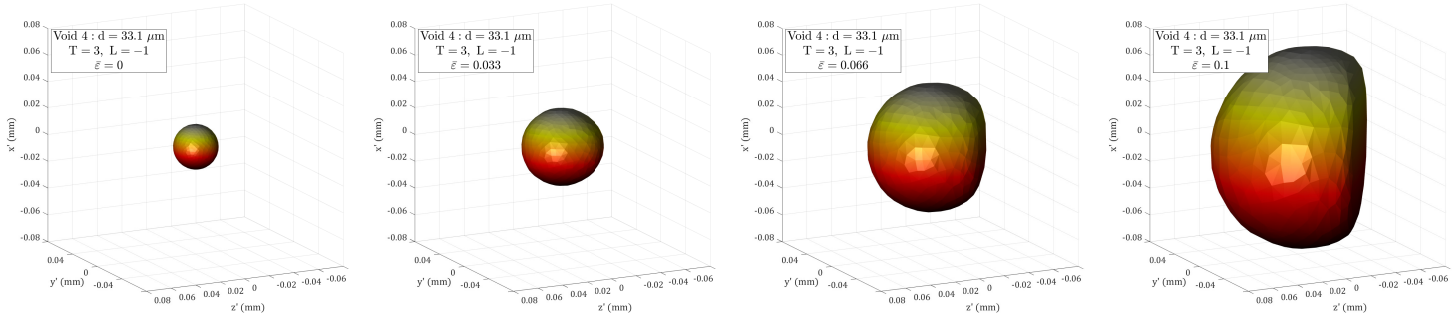

(a) (b) (c) (d)

Figure 7: Results corresponding to porous microstructure INC1Z and realization R1 for stress triaxiality $T = 3$ and Lode parameter $L = -1$. 3D reconstruction of the surface of void 4 included in Fig. 5b with initial diameter $d = 33.1$ μm for different values of the macroscopic effective strain: (a) $\bar{\varepsilon} = 0$, (b) $\bar{\varepsilon} = 0.033$, (c) $\bar{\varepsilon} = 0.066$ and (d) $\bar{\varepsilon} = 0.1$. The origin of the Cartesian coordinate system (x', y', z') is located at the center of mass of the void, with x', y' and z' being parallel to the loading axes x, y and z.

4.2. The effect of stress triaxiality

Fig. 8 compares results for the evolution of the normalized macroscopic effective stress $\bar{\Sigma}/\sigma_0$ versus the macroscopic effective strain $\bar{\varepsilon}$, for calculations performed with $L = -1$ and three different values of stress triaxiality, $T = 1$, 2 and 3. Realization R4 has been chosen arbitrarily, as we have checked that the same qualitative results are obtained for any other realization (all the results shown in Section 4.2 correspond to R4 and $L = -1$). The macroscopic stress is an increasing function of the macroscopic strain for the lowest triaxiality considered $T = 1$, for the range of macroscopic strains investigated. In contrast, the $\bar{\Sigma}/\sigma_0 - \bar{\varepsilon}$ curves for $T = 2$ and 3 show a maximum for intermediate values of strain because increasing triaxiality favors porosity growth, thus promoting the early loss of load carrying capacity of the unit-cell (the same observations have been reported in different works, e.g., see Kim et al. (2004b, 2007)).

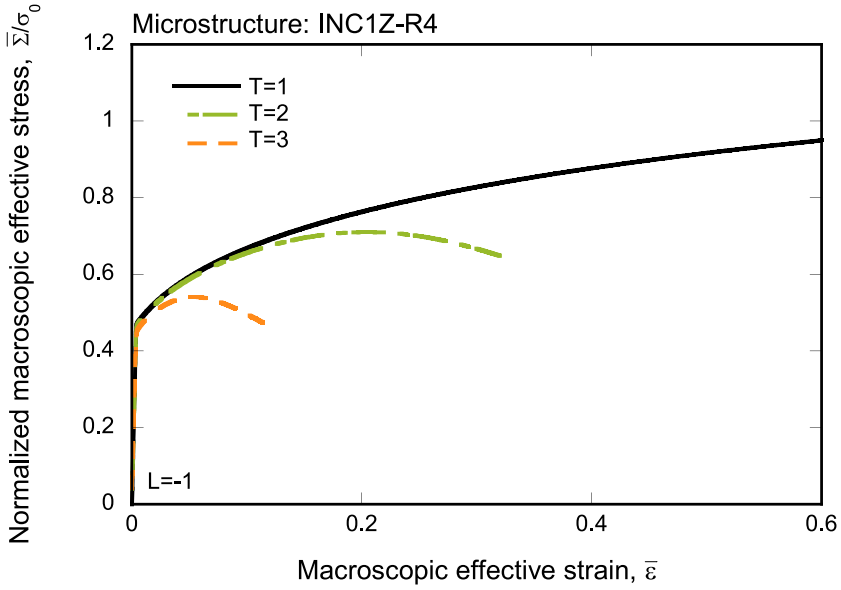

Figure 8: Results corresponding to porous microstructure INC1Z and realization R4 for Lode parameter $L = -1$ and three different values of the stress triaxiality, $T = 1$, 2 and 3. Normalized macroscopic effective stress $\bar{\Sigma}/\sigma_0$ versus macroscopic effective strain $\bar{\varepsilon}$.

Fig. 9 depicts the evolution of the volume of the five largest pores of the microstructure for calculations performed with two different values of the stress triaxiality, $T = 1$ and $T = 3$. The pores have initial diameters varying from 52.8 μm to 34.3 μm. The results corresponding to $T = 3$, see Fig. 9a, show that the evolution of the volume of the voids varies substantially from pore to pore, specially for macroscopic strains above 0.05 (in agreement with the results presented in Fig. 5 for realization R1). The pores growing faster and slower are voids 4 and 2, respectively. On the other hand, the calculations with $T = 1$, see Fig. 9b, show that the pores grow significantly less (the scale of the y-axis is eight times smaller), and that the differences between the $V^{\text{void}}/V_0^{\text{void}} - \bar{\varepsilon}$ curves are considerably smaller. In fact, perceptible differences in the volume of the voids appear only for macroscopic strains greater than 0.4 (later than in the

case of $T = 3$ for which the accelerated growth rate starts at ~ 0.05), void 4 being the pore that grows the slowest (while in the case of $T = 3$ void 4 was the fastest growing pore). It seems that decreasing triaxiality homogenizes the growth of the voids of the microstructure. We have checked that the same conclusion is obtained considering other sets of pores of this realization (the sets including five pores of intermediate size and the five smallest pores), and also considering various sets of pores of other realizations (R3 and R5).

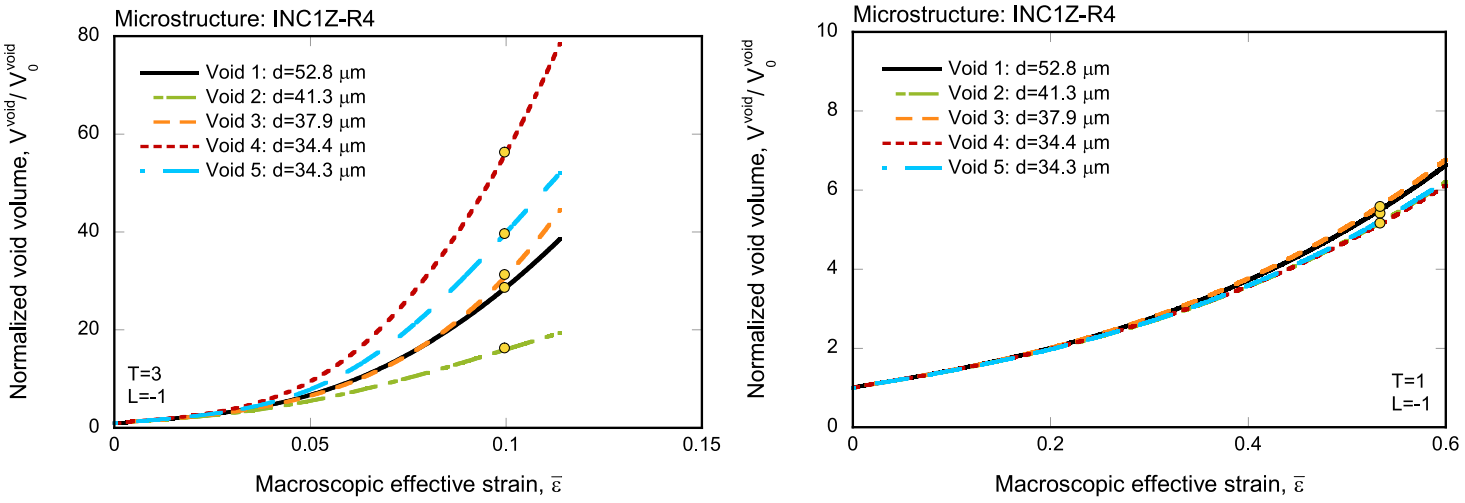

Figure 9: Results corresponding to porous microstructure INC1Z and realization R4 for Lode parameter $L = -1$ and different values of the stress triaxiality: (a) $T = 3$ and (c) $T = 1$. Normalized void volume $V^{\text{void}}/V_0^{\text{void}}$ versus macroscopic effective strain $\bar{\varepsilon}$ for the largest pores of the microstructure with diameters varying from 52.8 μm to 34.3 μm. The yellow markers indicate the macroscopic effective strains corresponding to the 3D reconstructions of the pores included in Figs. 10 and 11. (For interpretation of the references to color in this figure legend, the reader is referred to the web version of this article.)

The reconstruction of the voids of Fig. 9a for the stress triaxiality $T = 3$ and a macroscopic strain of 0.1 is shown in Fig. 10. The difference in size of the voids is apparent, and the shape also slightly varies from pore to pore, as the voids are no longer spherical due to the interaction with neighboring pores (the same conclusion obtained in Section 4.1). Recall that for this large value of triaxiality $T = 3$, the voids which do not interact with nearby pores tend to grow maintaining the spherical shape. The voids of Fig. 9b in the case of $T = 1$ and for a macroscopic strain of 0.533 are shown in Fig. 11. The pores are elongated along the major loading direction due to the lower imposed triaxiality, all showing similar shape and size. The comparison between Figs. 10 and 11 makes apparent that the volume of the pores is substantially smaller for the calculations with $T = 1$, despite the macroscopic strain is more than 5 times greater.

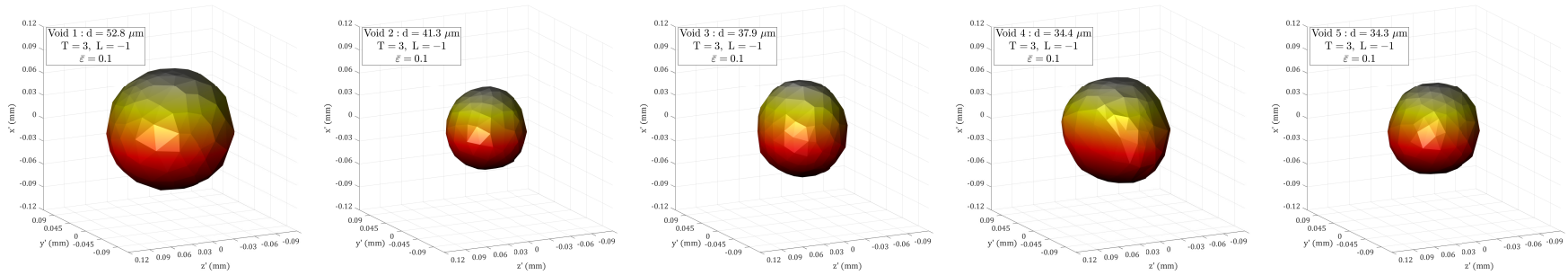

(a) (b) (c) (d) (e)

Figure 10: Results corresponding to porous microstructure INC1Z and realization R4 for stress triaxiality $T = 3$ and Lode parameter $L = -1$. 3D reconstruction of the surface of the largest pores of the microstructure for macroscopic effective strain $\bar{\varepsilon} = 0.1$: (a) void 1 with initial diameter $d = 52.8$ μm, (b) void 2 with initial diameter $d = 41.3$ μm, (c) void 3 with initial diameter $d = 37.9$ μm, (d) void 4 with initial diameter $d = 34.4$ μm and (e) void 5 with initial diameter $d = 34.3$ μm. The origin of the Cartesian coordinate system (x', y', z') is located at the center of mass of the void, with x', y' and z' being parallel to the loading axes x, y and z.

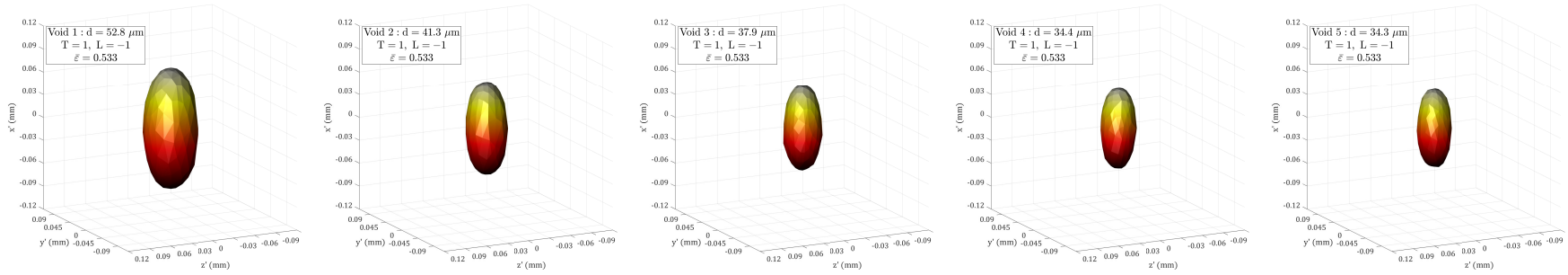

(a) (b) (c) (d) (e)

Figure 11: Results corresponding to porous microstructure INC1Z and realization R4 for stress triaxiality $T = 1$ and Lode parameter $L = -1$. 3D reconstruction of the surface of the largest pores of the microstructure for macroscopic effective strain $\bar{\varepsilon} = 0.533$: (a) void 1 with initial diameter $d = 52.8$ μm, (b) void 2 with initial diameter $d = 41.3$ μm, (c) void 3 with initial diameter $d = 37.9$ μm, (d) void 4 with initial diameter $d = 34.4$ μm and (e) void 5 with initial diameter $d = 34.3$ μm. The origin of the Cartesian coordinate system (x', y', z') is located at the center of mass of the void, with x', y' and z' being parallel to the loading axes x, y and z.

4.3. The effect of Lode parameter

Fig. 12 shows calculations performed with three different values of the Lode parameter, $L = -1$, 0 and 1. The stress triaxiality is $T = 3$ and the microstructural realization is R4 (all the results included in Section 4.3 correspond to R4 and $T = 3$). Fig. 12a includes the evolution of the normalized macroscopic effective stress $\bar{\Sigma}/\sigma_0$ with the macroscopic effective strain $\bar{\varepsilon}$. Varying the Lode parameter from -1, to 0 and 1 shifts the $\bar{\Sigma}/\sigma_0 - \bar{\varepsilon}$ curves upwards, delaying the drop of the stress and slowing down the strain softening process. The evolution of the normalized void volume fraction is shown in Fig. 12b. The fastest porosity growth corresponds to $L = -1$, and the slowest to 1, i. e., the order of the $f/f_0 - \bar{\varepsilon}$ curves is the opposite of the macroscopic effective stress (compare Figs. 12a and 12b), which illustrates that increasing porosity leads to earlier and more rapid strain localization process. We have checked that the same effect of the Lode parameter on the porosity growth is obtained for other realizations and triaxiality values investigated in this paper.

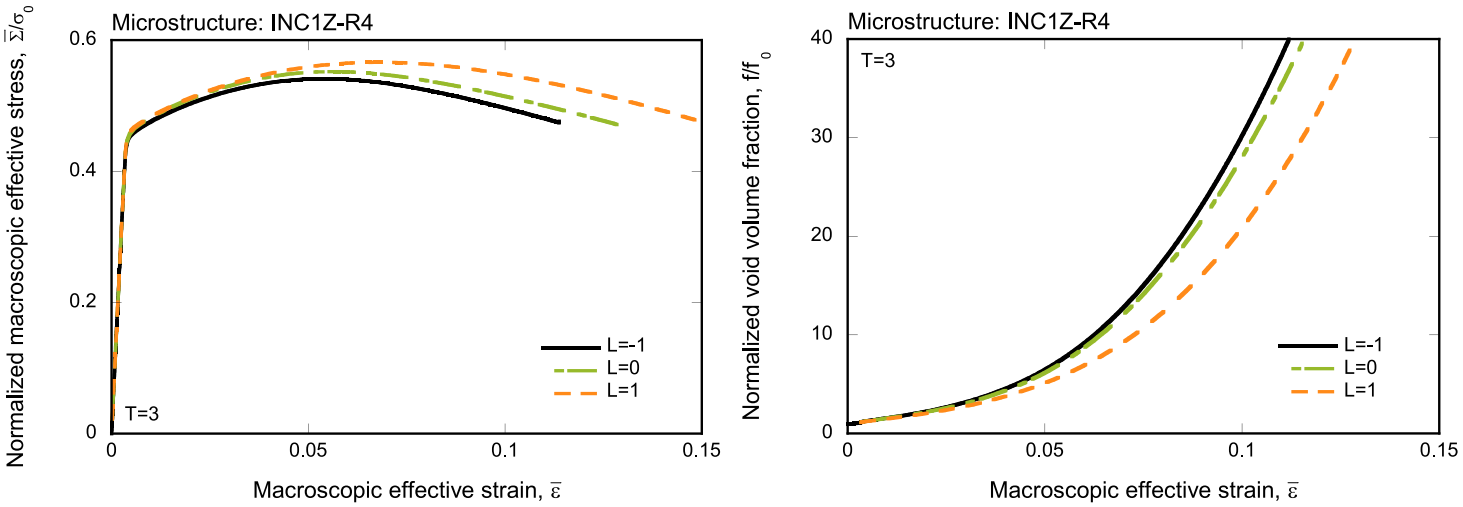

Figure 12: Results corresponding to porous microstructure INC1Z and realization R4 for stress triaxiality $T = 3$ and three different values of the Lode parameter $L = -1$, 0 and 1. (a) Normalized macroscopic effective stress $\bar{\Sigma}/\sigma_0$ versus macroscopic effective strain $\bar{\varepsilon}$. (b) Normalized void volume fraction f/f_0 versus macroscopic effective strain $\bar{\varepsilon}$.

Fig. 13 shows the evolution of the five largest pores of the microstructure, which have initial diameter varying from 52.8 μm to 34.3 μm (see also Section 4.2). The results corresponding to $L = 0$ are included in Fig. 13a, while Fig. 13b presents the data obtained with $L = 1$. Note that the order of the $V^{\text{void}}/V_0^{\text{void}} - \bar{\varepsilon}$ curves is different for both Lode parameters, showing that the stress state affects the relative growth of the pores and their collective behavior during loading. In addition, varying the Lode parameter from 0 to 1 leads to more uniform growth of the voids, as the $V^{\text{void}}/V_0^{\text{void}} - \bar{\varepsilon}$ curves are closer to each other (similar trends have been obtained for other realizations and triaxiality

values). The same qualitative results are obtained comparing the five smallest pores of the microstructure, which all have the same initial size $d = 7.4$ μm, see Fig. 14. For $L = 0$ the pore growing the fastest is void 5, Fig. 14a, showing a significant volume increase for values of the macroscopic effective strain greater than 0.05. In contrast, for Lode parameter 1, Fig. 14b, void 5 grows slower than voids 2 and 3, and the difference in the rate of growth between the fastest and the slowest growing pores is less than in the case of $L = 0$ (i.e., for $L = 1$ the slowest/fastest growing void grows faster/slower than in the case of $L = 0$).

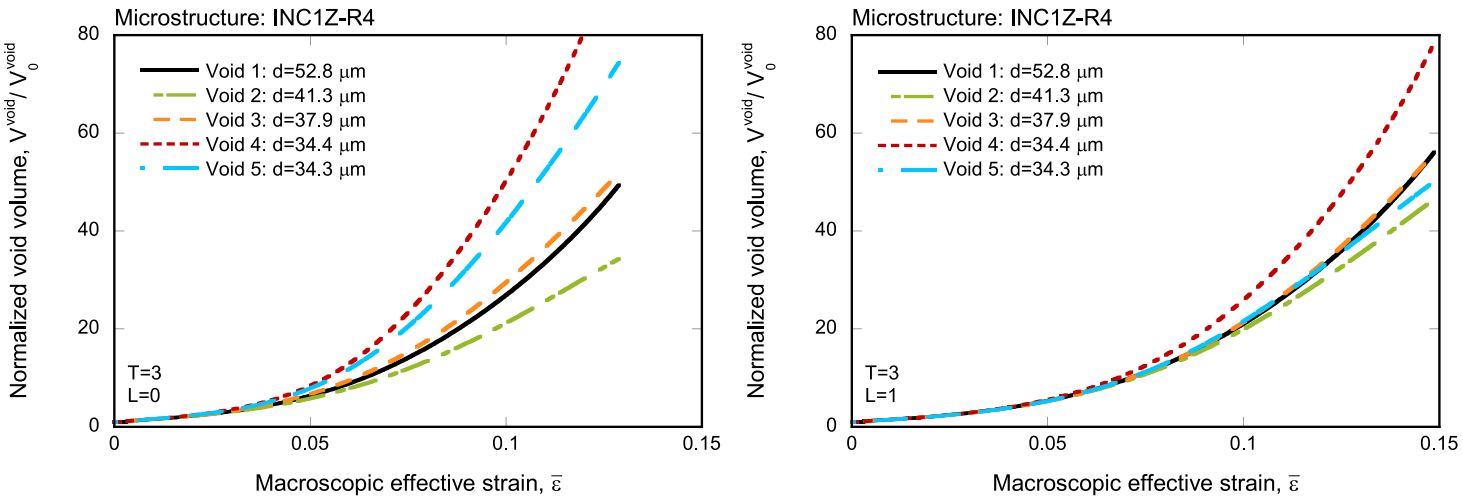

Figure 13: Results corresponding to porous microstructure INC1Z and realization R4 for stress triaxiality $T = 3$ and different values of the Lode parameter: (a) $L = 0$ and (b) $L = 1$. Normalized void volume $V^{\text{void}}/V_0^{\text{void}}$ versus macroscopic effective strain $\bar{\varepsilon}$ for the largest pores of the microstructure with diameters varying from 52.8 μm to 34.3 μm.

The increased uniformity in the pores size while varying the Lode parameter from 0 to 1 is further illustrated in Figs. 15 and 16 which show 3D reconstructions of the voids included in Figs. 14a and 14b, respectively. The pictures are taken for a macroscopic effective strain of 0.093 (see the yellow markers in Figs. 14a and 14b). For the case of $L = 0$, the size of voids 2 and 5 stands out with respect to the others, see Fig. 15, while for the Lode parameter 1 the size of the pores is noticeably more similar, see Fig. 16, since voids 2 and 5 have grown less, and the size of voids 1 and 4 is comparatively greater.

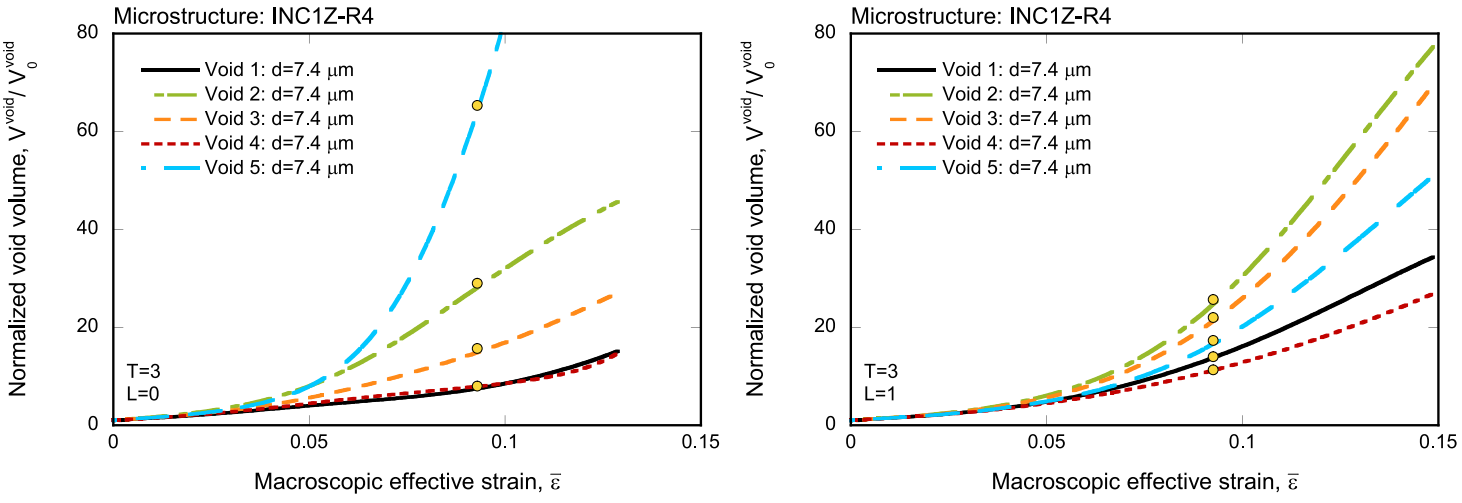

Figure 14: Results corresponding to porous microstructure INC1Z and realization R4 for stress triaxiality $T = 3$ and different values of the Lode parameter: (a) $L = 0$ and (b) $L = 1$. Normalized void volume $V^{\text{void}}/V_0^{\text{void}}$ versus macroscopic effective strain $\bar{\varepsilon}$ for the smallest pores of the microstructure with diameter 7.4 μm. The yellow markers indicate the macroscopic effective strains corresponding to the 3D reconstructions of the pores included in Figs. 15 and 16. (For interpretation of the references to color in this figure legend, the reader is referred to the web version of this article.)

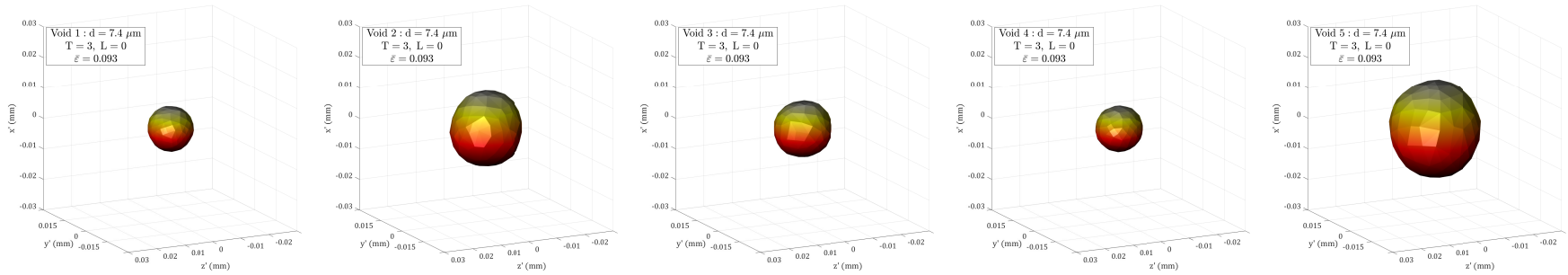

(a) (b) (c) (d) (e)

Figure 15: Results corresponding to porous microstructure INC1Z and realization R4 for stress triaxiality $T = 3$ and Lode parameter $L = 0$. 3D reconstruction of the surface of the smallest pores of the microstructure for macroscopic effective strain $\bar{\varepsilon} = 0.093$: (a) void 1 with initial diameter $d = 7.4$ μm, (b) void 2 with initial diameter $d = 7.4$ μm, (c) void 3 with initial diameter $d = 7.4$ μm, (d) void 4 with initial diameter $d = 7.4$ μm and (e) void 5 with initial diameter $d = 7.4$ μm. The origin of the Cartesian coordinate system (x', y', z') is located at the center of mass of the void, with x', y' and z' being parallel to the loading axes x, y and z.

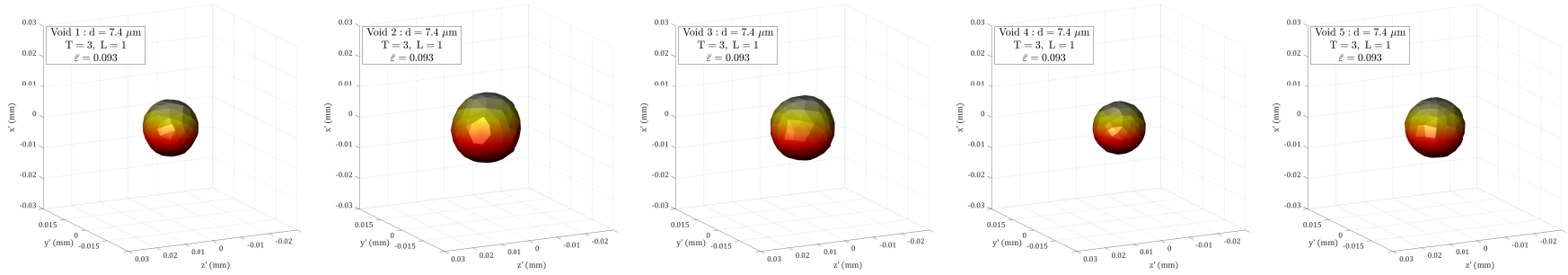

(a) (b) (c) (d) (e)

Figure 16: Results corresponding to porous microstructure INC1Z and realization R4 for stress triaxiality $T = 3$ and Lode parameter $L = 1$. 3D reconstruction of the surface of the smallest pores of the microstructure for macroscopic effective strain $\bar{\varepsilon} = 0.093$: (a) void 1 with initial diameter $d = 7.4$ μm, (b) void 2 with initial diameter $d = 7.4$ μm, (c) void 3 with initial diameter $d = 7.4$ μm, (d) void 4 with initial diameter $d = 7.4$ μm and (e) void 5 with initial diameter $d = 7.4$ μm. The origin of the Cartesian coordinate system (x', y', z') is located at the center of mass of the void, with x', y' and z' being parallel to the loading axes x, y and z.

5. Parametric analysis

The calculations correspond to macroscopic stress triaxiality $T = 3$ and Lode parameter $L = -1$. Section 5.1 compares results obtained for microstructures Al3XY and SS5XY (the microstructures which were not considered in Section 4), which display large differences in void volume fraction and pores size distribution, see Tables 2 and 3. Moreover, the effect of void volume fraction is investigated in Section 5.2 taking the distribution of void sizes of microstructure INC1Z as a reference and performing calculations with different values of initial porosity. On the other hand, Section 5.3 presents calculations with the initial void volume fraction of microstructure INC1Z but different distributions of void sizes obtained by varying the mean and the standard deviation of the Log-normal function used to fit the experimental data, see Table 2.

5.1. The effect of porous microstructure

Fig. 17 compares results for porous microstructures Al3XY-R1 and SS5XY-R1. Recall from Section 3 that the initial void volume fraction of Al3XY-R1 is ≈ 300 times greater, and that the pores of SS5XY-R1 are smaller (see Tables 2 and 3). Calculations performed modeling the mechanical behavior of the unit-cell using Gurson (1977) porous plasticity are also included (with the same initial void volume fraction of the calculations with actual pores).

Fig. 17a shows the evolution of the macroscopic effective stress $\bar{\Sigma}/\sigma_0$ with the macroscopic effective strain $\bar{\varepsilon}$. The initial yield stress and the maximum effective stress are lower for microstructure Al3XY-R1, and the strain softening process starts at smaller value of strain. In contrast, the void volume fraction grows faster for SS5XY-R1, see Fig. 17b, suggesting that decreasing the initial porosity boosts the normalized rate of growth of the void volume fraction (as further confirmed in Section 5.2). Notice that the same qualitative results are obtained for the calculations with actual porosity and homogenized porosity (Gurson model). However, for the microstructure Al3XY-R1, the Gurson model predicts slower strain softening and roughly the same void volume fraction evolution. On the other hand, for the microstructure SS5XY-R1, the Gurson model displays faster strain softening and much greater porosity growth. These results make apparent that initial void volume fraction and spatial and size distribution of voids play an important role on the effective mechanical properties of the porous aggregate and on the evolution of the porous microstructure.

Fig. 18 shows contours of effective plastic strain in the matrix material for the calculations with actual voids included in Fig. 17. The pictures of Al3XY-R1 correspond to $\bar{\varepsilon} = 0$ and 0.033, while in the case of SS5XY-R1 the contours for $\bar{\varepsilon} = 0.066$, 0.1 and 0.133 are also included since the drop of the stress starts at larger strain. The microstructure Al3XY-R1 contains a large amount of pores, which are relatively close to each other, so that the voids start to interact shortly

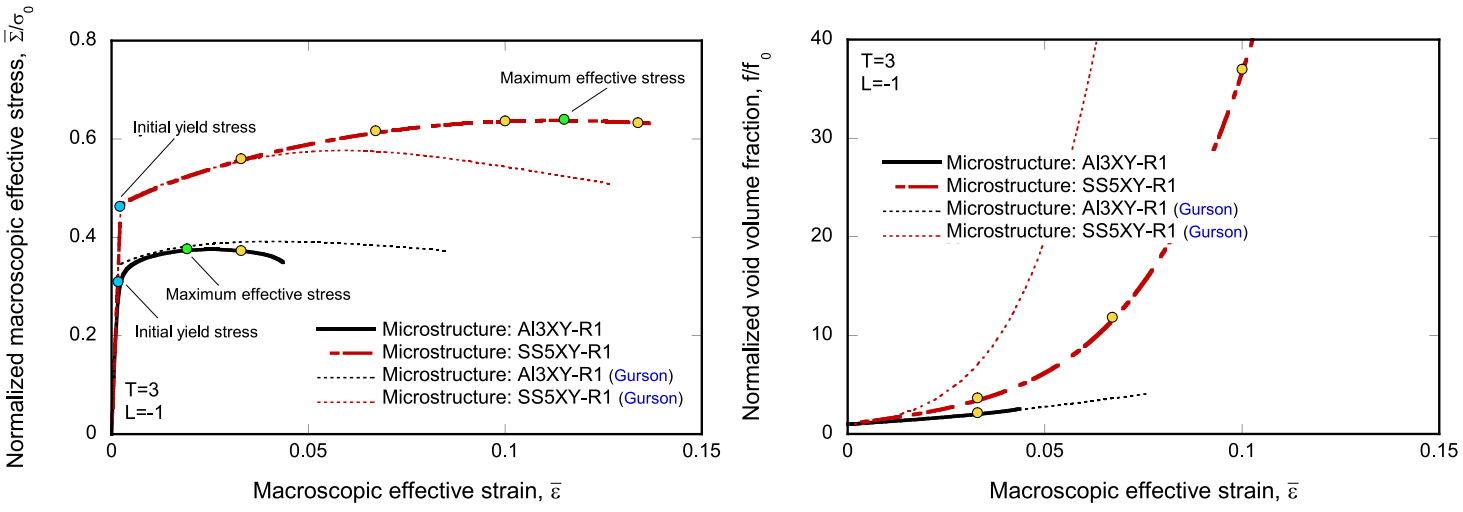

Figure 17: Porous microstructures Al3XY-R1 and SS5XY-R1. Results for stress triaxiality $T = 3$ and Lode parameter $L = -1$. Comparison between results obtained with actual voids and with Gurson (1977) porous plasticity. (a) Normalized macroscopic effective stress $\bar{\Sigma}/\sigma_0$ versus macroscopic effective strain $\bar{\varepsilon}$. (b) Normalized void volume fraction f/f_0 versus macroscopic effective strain $\bar{\varepsilon}$. The yellow markers correspond to different values of the macroscopic effective strain $\bar{\varepsilon} = 0.033$, 0.066, 0.1 and 0.133 shown in the contour plots of Fig. 18. (For interpretation of the references to color in this figure legend, the reader is referred to the web version of this article.)

after the beginning of loading, with plastic strains localizing between the voids –coalescence localization of the voids–, despite the mild growth of the pores (for $\bar{\varepsilon} = 0.033$ the void volume fraction is *only* twice the initial, yet the effective stress is already decreasing, see Fig. 17a). On the other hand, notice that, while in the case of SS5XY-R1 the number of pores is less and they grow faster (for $\bar{\varepsilon} = 0.033$ the void volume fraction is 3.6 times the initial, see Fig. 17b), the localization of plastic deformation is generally circumscribed to a narrow region near the surface of the voids, suggesting lesser interaction between the pores, as some of the voids seem to be *virtually isolated* in the matrix material.

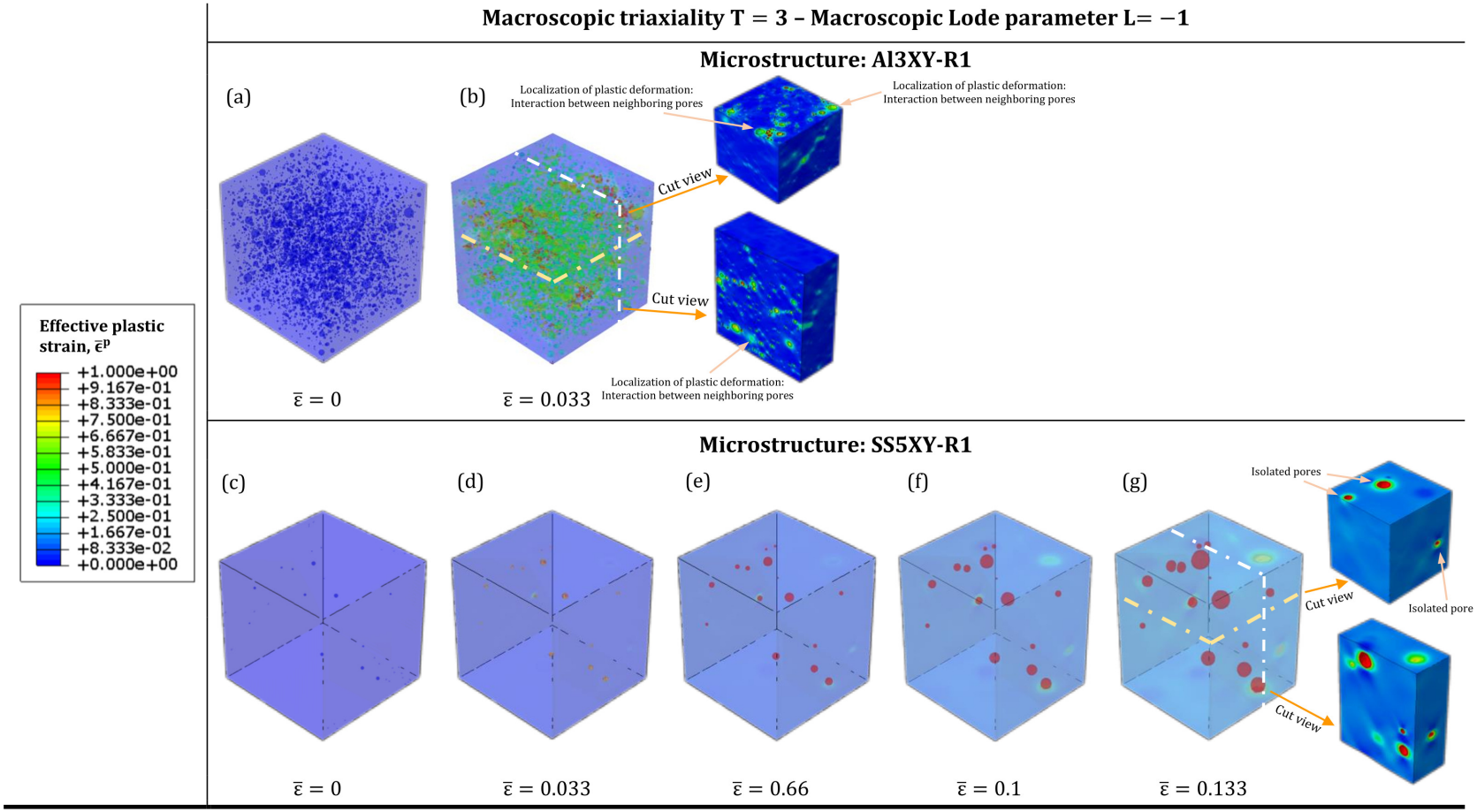

Figure 18: Results corresponding to stress triaxiality $T = 3$ and Lode parameter $L = -1$. Contours of effective plastic strain in the matrix material $\bar{\epsilon}^p$ for different values of macroscopic effective strain $\bar{\varepsilon} = 0, 0.033$, 0.066, 0.1 and 0.133. (a)-(b) Porous microstructure Al3XY-R1. (c)-(g) Porous microstructure SS5XY-R1.

5.2. The effect of void volume fraction

Fig. 19 includes finite element results for calculations performed with actual voids and with homogenized porosity (Gurson model), for unit-cells with two initial void volume fractions, $f_0 = 0.5\%$ and 1%. The parent microstructure is INC1Z, i.e., in the calculations with actual pores the voids size distribution meets the maximum and minimum void size, and the mean and the standard deviation given in Table 2. The number of voids for the microstructure with $f_0 = 0.5\%$ is 957, while in the case of $f_0 = 1\%$ the number of pores is 1917 (roughly double). Results for a calculation with a single pore in the center of the unit-cell are also included.

The evolution of the macroscopic effective stress is included in Fig. 19a. The calculations with multiple voids show that increasing the initial void volume fraction shifts the $\bar{\Sigma}/\sigma_0 - \bar{\varepsilon}$ curve downwards, and speeds up the strain softening process, consistent with the conclusions obtained in Section 5.1 for the calculations performed with microstructures Al3XY-R1 and SS5XY-R1. The simulations with a single void and with Gurson (1977) plasticity yield similar results, but the strain softening is slower and more progressive. Moreover, Fig. 19b shows that there is a qualitative agreement for the void volume fraction evolution between actual porosity, single void, and homogenized porosity simulations. The growth of the normalized porosity is faster for the microstructure with lower initial void volume fraction $f_0 = 0.5\%$, which also confirms the conclusions obtained from the calculations presented in Section 5.1. However, there are quantitative differences between the results obtained with the three different approaches for the porosity growth, so that the unit-cells with a single void display lower rate of void volume fraction growth.

Despite the microstructure with 1% of initial porosity contains more voids, they generally grow slower (normalized growth rate of the voids). Figs. 20a and 20b show the evolution of the normalized volume of the five largest voids of the microstructure for the calculations with multiple voids and $f_0 = 0.5\%$ and $f_0 = 1\%$, respectively. The initial diameter of the voids varies from 69.9 μm to 62.4 μm. Note that the fastest/slowest growing pore for $f_0 = 0.5\%$ grows faster than the fastest/slowest growing pore for $f_0 = 1\%$. The same qualitative results are obtained comparing the evolution of the normalized volume of the five smallest voids of the microstructure, which all have initial diameter of 7.4 μm, see Figs. 21a and 21b. The differences in the results between the unit-cells with 0.5% and 1% of initial porosity are apparent, as in the latter case, four out of the five pores considered have a normalized volume smaller/equal than 3 for a macroscopic strain of 0.6, with the volume of void 2 increasing *only* by 20%. The same general trends have been obtained using SS5XY as parent microstructure, performing calculations with initial void volume fractions of 0.5% and 1% (results are not shown for the sake of brevity), which seems to confirm that increasing the porosity generally slows

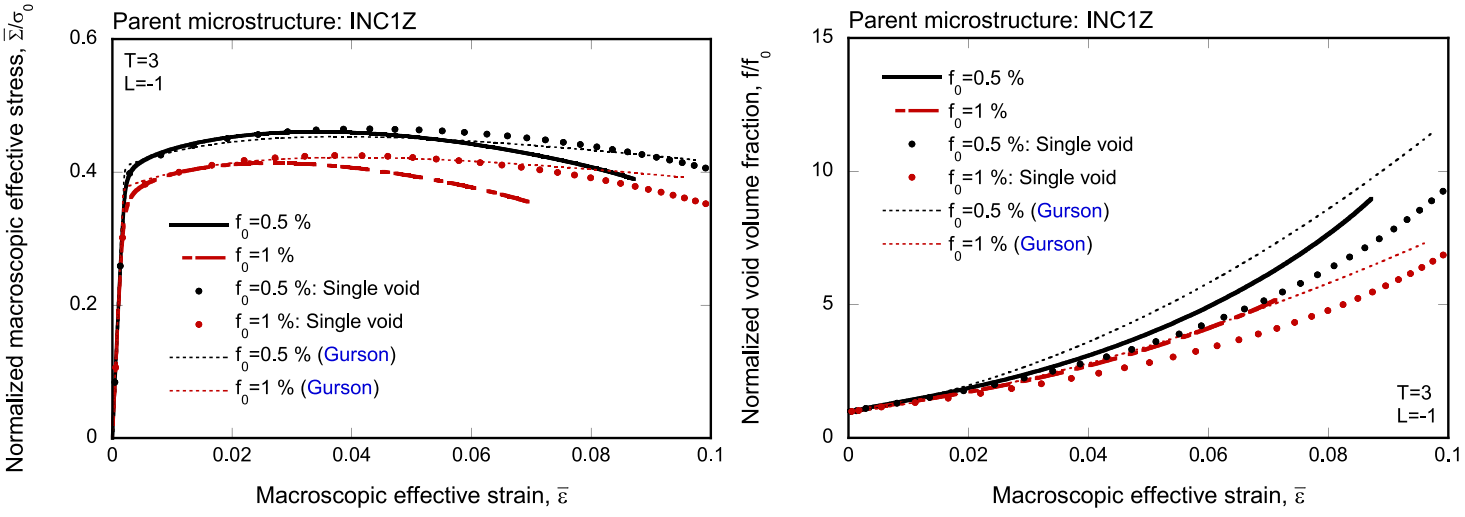

Figure 19: Parent porous microstructure INC1Z. Results for two different initial void volume fractions $f_0 = 0.5\%$ and $f_0 = 1\%$, for stress triaxiality $T = 3$ and Lode parameter $L = -1$. Comparison between results obtained with actual voids, single void and Gurson (1977) porous plasticity. (a) Normalized macroscopic effective stress $\bar{\Sigma}/\sigma_0$ versus macroscopic effective strain $\bar{\varepsilon}$. (b) Normalized void volume fraction f/f_0 versus macroscopic effective strain $\bar{\varepsilon}$.

down the normalized growth rate of the voids.

5.3. The effect of voids size

Fig. 22 includes calculations with multiple voids performed for three porous microstructures with different values of the mean voids size, $\mu = 10$ μm, 30 μm and 50 μm. The parent microstructure is INC1Z, i.e., the void size distribution meets the initial void volume fraction and the standard deviation given in Table 2. The number of voids for the microstructures with $\mu = 10$ μm, 30 μm and 50 μm is 1633, 61 and 14, respectively, and the diameter of the largest void is 28.8 μm, 71.89 μm and 84.00 μm. The results obtained with actual voids are compared with a calculation in which the mechanical behavior of the material is modeled with Gurson plasticity (homogenized porosity) and the same value of initial void volume fraction ($f_0 = 0.13\%$). Results for a calculation with a single pore in the center of the unit-cell are also included.

Fig. 22a shows the evolution of the macroscopic effective stress with the macroscopic effective strain. The influence of the mean voids size on the $\bar{\Sigma}/\sigma_0 - \bar{\varepsilon}$ curves becomes noticeable during the strain softening process, which is faster for the intermediate value $\mu = 30$ μm (i.e., in these calculations there is no direct correlation between the mean voids size and the rate of strain softening). Note that the calculation using a single void predicts very similar results to the simulation with $\mu = 50$ μm, while the calculation with Gurson plasticity yields lower effective stress and slower strain softening process than the unit-cells with multiple voids. Fig. 22b shows the evolution of the void volume fraction with

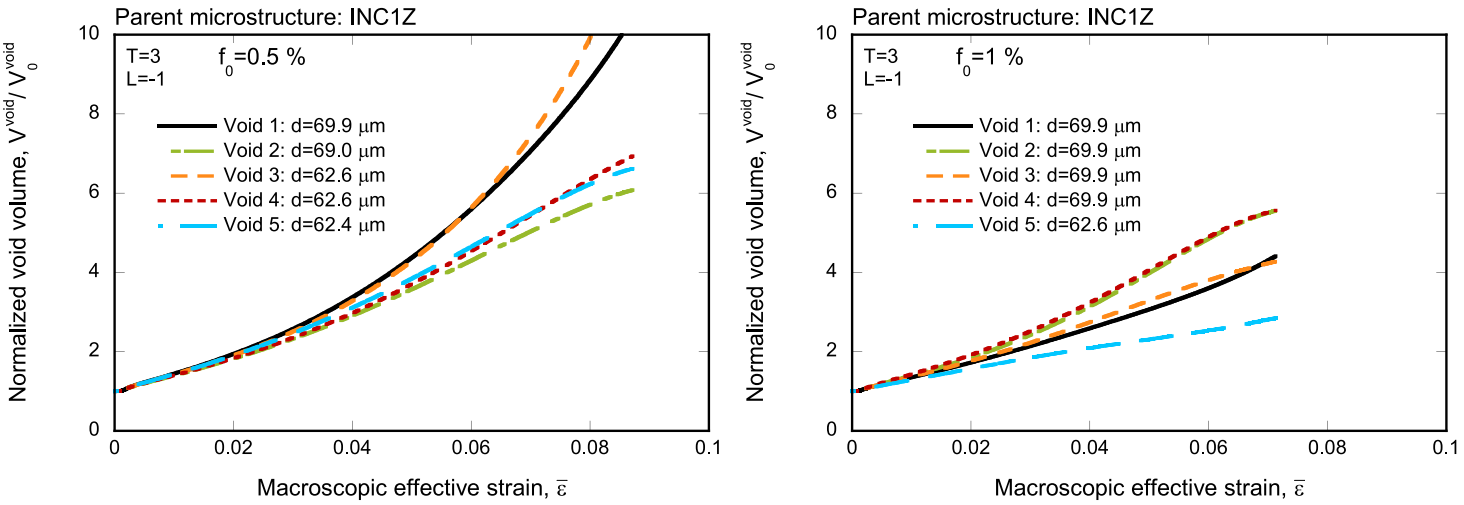

Figure 20: Parent porous microstructure INC1Z. Results for stress triaxiality $T = 3$ and Lode parameter $L = -1$. Normalized void volume $V^{\text{void}}/V_0^{\text{void}}$ versus macroscopic effective strain $\bar{\varepsilon}$ for the largest pores of the microstructure with diameters varying from 69.9 μm to 62.4 μm. Two different initial volume fractions: (a) $f_0 = 0.5\%$ and (b) $f_0 = 1\%$.

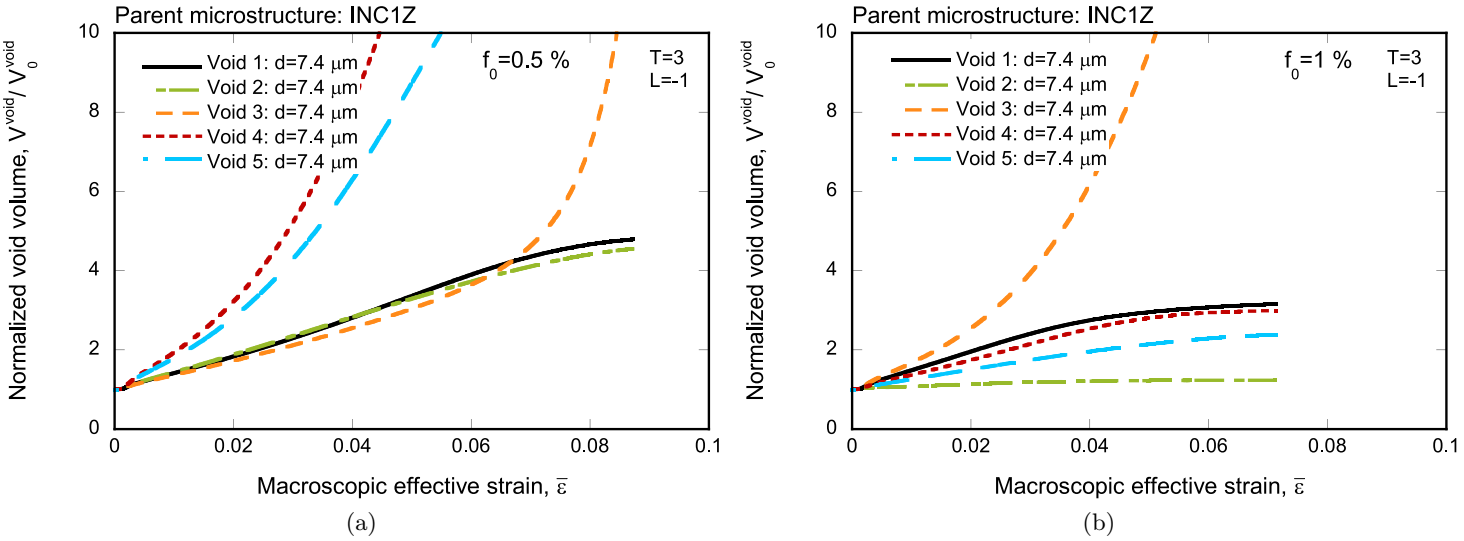

Figure 21: Parent porous microstructure INC1Z. Results for stress triaxiality $T = 3$ and Lode parameter $L = -1$. Normalized void volume $V^{\text{void}}/V_0^{\text{void}}$ versus macroscopic effective strain $\bar{\varepsilon}$ for the smallest pores of the microstructure with diameter 7.4 μm. Two different initial volume fractions: (a) $f_0 = 0.5\%$ and (b) $f_0 = 1\%$.

the macroscopic effective strain. The effect of μ on the $f/f_0 - \bar{\varepsilon}$ curves computed with multiple voids is such that the porosity grows faster as the calculation shows lower effective stress and faster strain softening (compare Figs. 22a and 22b). Notice that the differences in the void volume fraction evolution for the calculations with multiple voids increase with the macroscopic strain. Notice also that the $f/f_0 - \bar{\varepsilon}$ curve obtained with a single pore lies within the results obtained with the calculations with multiple voids, while Gurson plasticity predicts significantly faster porosity growth. The large differences in the number and size of the pores between the microstructures with mean voids size $\mu = 10$ μm, 30 μm and 50 μm are illustrated in the contours of effective plastic strain shown in Fig. 23 for different macroscopic effective strains $\bar{\varepsilon} = 0$, 0.033 and 0.066 (corresponding to the yellow markers in Fig. 22). As the mean void size increases, there are less but larger pores. The comparison of the cut-views in pictures (c) and (i) shows that for $\mu = 50$ μm the plastic deformation mostly localizes surrounding large pores, while in the case of $\mu = 10$ μm there are many localization bands connecting a multitude of small nearby voids.

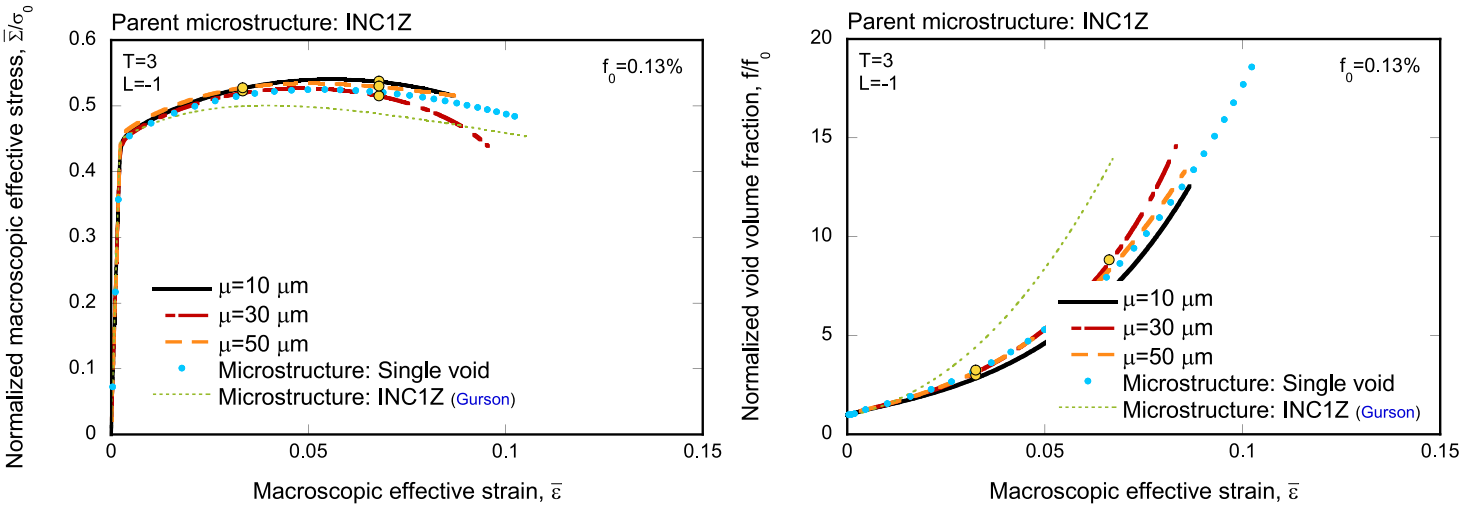

Figure 22: Parent porous microstructure INC1Z. Results for three different values of the mean voids size $\mu = 10$ μm, $\mu = 30$ μm and $\mu = 50$ μm, for stress triaxiality $T = 3$ and Lode parameter $L = -1$. Comparison between results obtained with actual voids, single void and Gurson (1977) porous plasticity. The initial void volume fraction is $f_0 = 0.13\%$. (a) Normalized macroscopic effective stress $\bar{\Sigma}/\sigma_0$ versus macroscopic effective strain $\bar{\varepsilon}$. (b) Normalized void volume fraction f/f_0 versus macroscopic effective strain $\bar{\varepsilon}$. The yellow markers correspond to different values of the macroscopic effective strain shown in the contour plots of Fig. 23. (For interpretation of the references to color in this figure legend, the reader is referred to the web version of this article.)

Fig. 24 shows finite element simulations with actual voids for three different values of the standard deviation of the pores size distribution, $SD = 3$ μm, 10 μm and 15 μm. The parent microstructure is INC1Z, i.e., the void size distribution meets the initial void volume fraction and the mean void size given in Table 2. The number of voids for the microstructures with $SD = 3$ μm, $SD = 10$ μm and $SD = 15$ μm is 517, 143 and 87, respectively, and the diameter of the largest void is 25.60 μm, 105.43 μm and 110.03 μm. The results obtained with multiple voids are compared with a

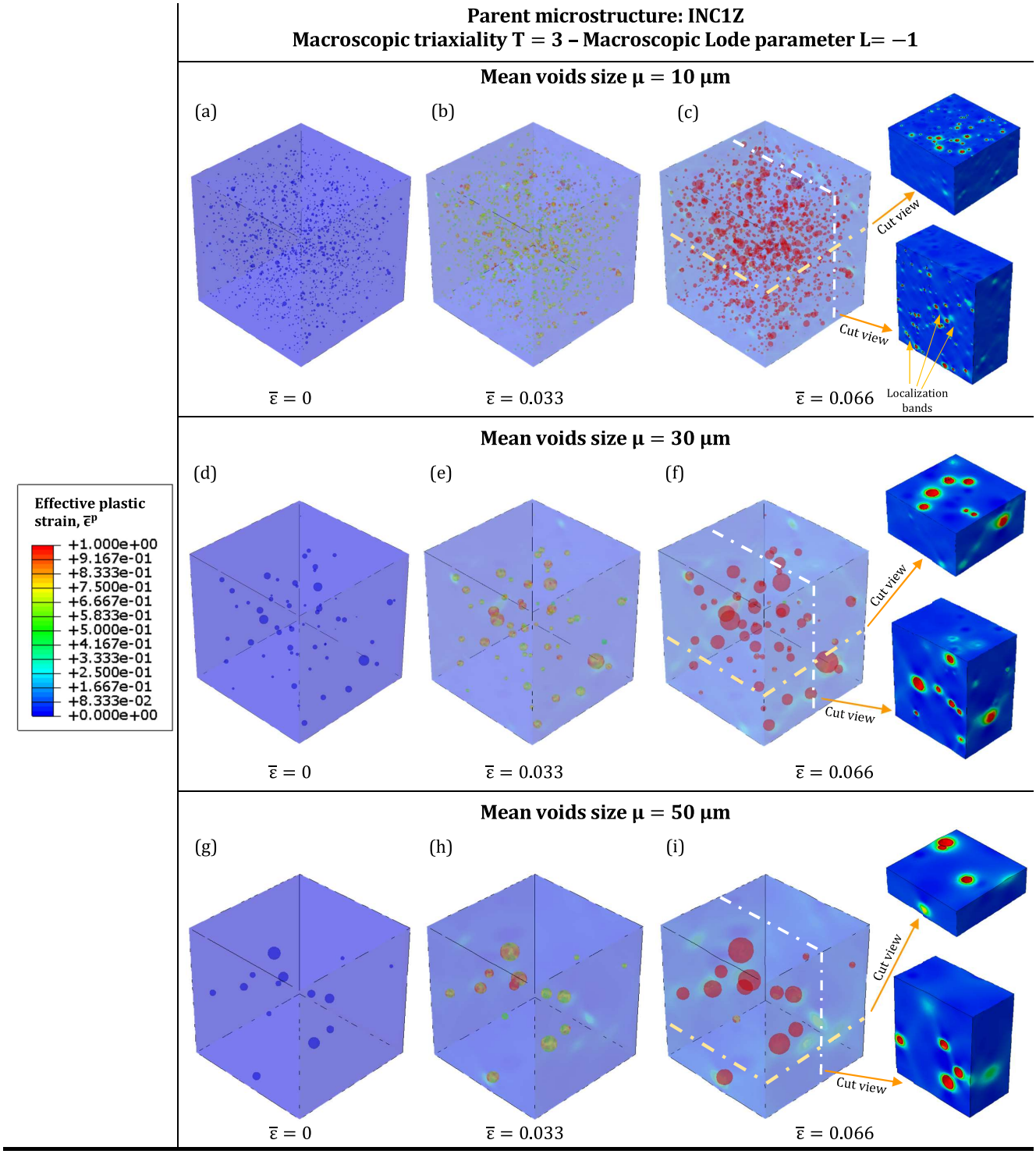

Figure 23: Results corresponding to parent porous microstructure INC1Z for stress triaxiality $T = 3$ and Lode parameter $L = -1$. The initial void volume fraction is $f_0 = 0.13\%$. Contours of effective plastic strain in the matrix material $\bar{\epsilon}^p$ for different values of macroscopic effective strain $\bar{\varepsilon} = 0, 0.05$ and 0.1. (a)-(c) Mean voids size $\mu = 10$ μm. (d)-(f) Mean voids size $\mu = 30$ μm. (g)-(i) Mean voids size $\mu = 50$ μm. (For interpretation of the references to color in this figure legend, the reader is referred to the web version of this article.)

calculation which includes a single pore in the center of the unit-cell, and with a calculation in which the mechanical behavior of the material is modeled with Gurson plasticity.

The evolution of the macroscopic effective stress is included in Fig. 24a. Increasing the standard deviation of the distribution of void sizes to $SD = 15$ μm leads to faster strain softening (the results for $SD = 3$ μm and 10 μm are very similar). For the calculation with a single central pore, the strain softening process is slowed down compared to the calculations with multiple pores, while in the case of the unit-cell modeled with Gurson plasticity, the strain softening starts earlier in the loading process. The evolution of the void volume fraction is shown in Fig. 24b. For the calculations with multiple voids, the faster porosity growth corresponds to $SD = 15$ μm (which explains the increased softening in Fig. 24a). Moreover, the void volume fraction grows slower at large strains for the simulation with a single pore than for the unit-cells with multiple pores, while in the case of modeling the material with Gurson plasticity, the porosity grows faster than for any calculation with explicitly resolved voids. These simulations reinforce the idea that an explicit description of the porous microstructure leads to important differences in the evolution of the void volume fraction with respect to calculations with homogenized porosity, and demonstrate that the differences in the $f/f_0 - \bar{\varepsilon}$ curves obtained from unit-cells with explicitly resolved pores increase with the macroscopic strain.

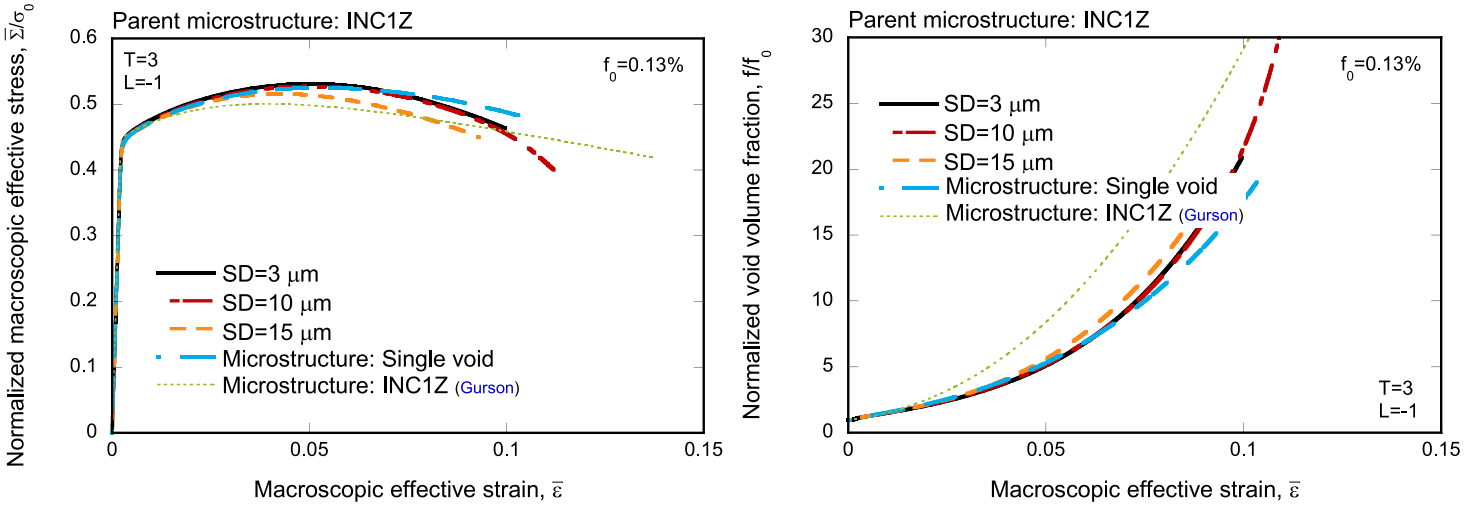

Figure 24: Parent porous microstructure INC1Z. Results for three different values of the standard deviation $SD = 3$ μm, $SD = 10$ μm and $SD = 15$ μm, for stress triaxiality $T = 3$ and Lode parameter $L = -1$. Comparison between results obtained with actual voids, single void and Gurson (1977) porous plasticity. The initial void volume fraction is $f_0 = 0.13\%$. (a) Normalized macroscopic effective stress $\bar{\Sigma}/\sigma_0$ versus macroscopic effective strain $\bar{\varepsilon}$. (b) Normalized void volume fraction f/f_0 versus macroscopic effective strain $\bar{\varepsilon}$. (For interpretation of the references to color in this figure legend, the reader is referred to the web version of this article.)

6. Clustering analysis

All the calculations in this section include multiple voids. Neither any comparison is performed with unit-cells with a single void, nor with simulations in which the mechanical behavior of the material is modeled with Gurson (1977) plasticity. Unlike in the calculations with actual voids included in Sections 4 and 5, in which the voids were randomly distributed in the unit-cell, in the simulations presented in this section the pores are packed into clusters. For that purpose, the center-satellite model developed by Graham-Brady (2010) to create microstructures with clusters of flaws in a 2D domain has been adapted to generate 3D microstructures with clusters of voids. The model assumes some fraction of all pores l act as center of clusters (parent voids) and the satellite pores (children voids) are contained within a sphere of radius R_c centered in the parent void. The number of parent voids in the microstructure follows a Poisson's distribution with parameter lN_vV^{cell}, where N_v is the number of voids per unit volume. The parent voids are distributed randomly in the unit-cell. For each parent void, the number of children voids is determined using a Poisson's distribution with parameter $\frac{1-l}{l}$.

The finite element simulations are performed with unit-cells containing three different number of clusters $N_c = 5$, 11 and 28, for macroscopic stress triaxiality $T = 3$ and Lode parameter $L = -1$. The parameters of the center-satellite model used to create the clustering microstructures are included in Table 4. The main features of the resulting porous microstructures are given in Table 5. Note that the parent microstructure is INC1Z, i.e., the voids size distribution meets the Log-normal distribution with mean and standard deviation given in Table 2. The initial void volume fraction for the three clustering microstructures is roughly the same.

	$N_c = 5$	$N_c = 11$	$N_c = 28$
l (%)	5	10	20
R_c (mm)	0.1	0.1	0.1
N_v (num./mm^3)	147	147	147

Table 4: Parameters of the center-satellite model used to create the clustering microstructures investigated in this work: fraction of pores acting as parent voids (l), radius of the sphere containing the children voids (R_c) and number of voids per unit volume (N_v).

Fig. 25 shows the evolution of the macroscopic effective stress and the void volume fraction with the macroscopic effective strain for the three clustering microstructures considered. The effective stress is little sensitive to changes in the number of clusters, yet, the $\bar{\Sigma}/\sigma_0 - \bar{\varepsilon}$ curve corresponding to $N_c = 5$ is shifted downwards compared to the microstructures with larger number of clusters, see Fig. 25a. This is most likely because decreasing the number of clusters speeds up

	$N_c = 5$	$N_c = 11$	$N_c = 28$
f_0 (%)	0.049	0.057	0.064
N_t (num.)	106	104	117
d_{max} (μm)	58.9	58.9	58.9
d_{min} (μm)	7.40	7.40	7.40

Table 5: Initial void volume fraction (f_0), number of voids (N_t), maximum void diameter (d_{max}) and minimum void diameter (d_{min}) in the finite element models corresponding to the clustering microstructures.

the growth of porosity, see Fig. 25b, which in turn leads to faster strain softening. We have also checked that the void volume fraction for $N_c = 5$ grows faster than for the five calculations included in Fig. 2b in which the pores were randomly distributed in the unit-cell (in contrast, the results for $N_c = 11$ and $N_c = 28$ lie within the $f/f_0 - \bar{\varepsilon}$ curves included in Fig. 2b). These results suggest that the relative position and interaction of voids in the microstructure affect the evolution of the void volume fraction. Namely, for a given voids size distribution, clustering of pores seems to favor porosity growth. This conclusion is further substantiated analyzing the evolution of the volume of the five largest pores of the three clustering microstructures, compare Figs. 26a, 26b and 26c. While different voids grow at different speeds, it is apparent that these graphs show a trend for the pores growing slower as the number of clusters increases (we have computed the average volume of the five pores for the three clustering microstructures and obtained the same qualitative results of Fig. 25b).

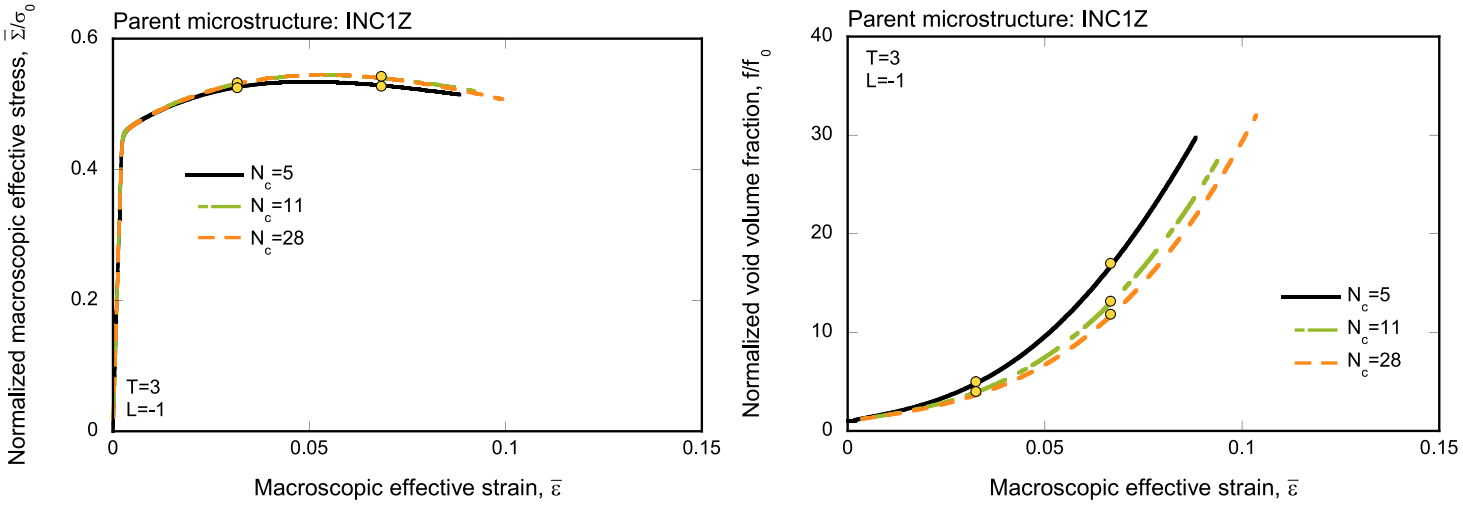

Figure 25: Parent porous microstructure INC1Z. Results for three different spatial distributions of voids with $N_c = 5$, $N_c = 11$ and $N_c = 28$ clusters, respectively. The stress triaxiality is $T = 3$ and the Lode parameter is $L = -1$. (a) Normalized macroscopic effective stress $\bar{\Sigma}/\sigma_0$ versus macroscopic effective strain $\bar{\varepsilon}$. (b) Normalized void volume fraction f/f_0 versus macroscopic effective strain $\bar{\varepsilon}$. The yellow markers correspond to two different values of the macroscopic effective strain $\bar{\varepsilon} = 0.033$ and 0.066 shown in the contour plots of Fig. 27. (For interpretation of the references to color in this figure legend, the reader is referred to the web version of this article.)

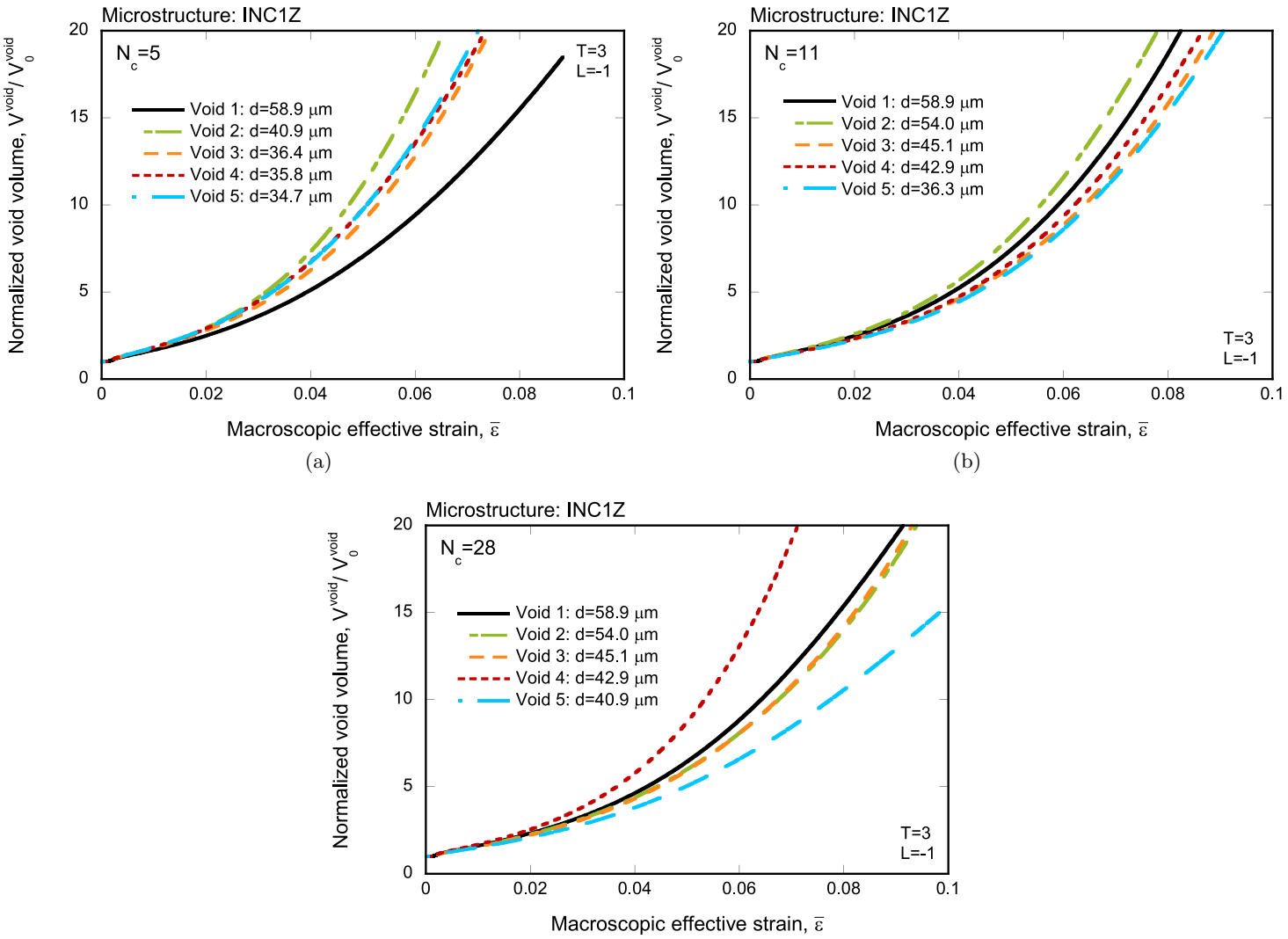

Figure 26: Parent porous microstructure INC1Z. Results for stress triaxiality $T = 3$ and Lode parameter $L = -1$. Normalized void volume $V^{\text{void}}/V_0^{\text{void}}$ versus macroscopic effective strain $\bar{\varepsilon}$ for the largest pores of the microstructure with diameters varying from 58.9 μm to 34.7 μm. Three different spatial distributions of voids with clusters: (a) $N_c = 5$, (b) $N_c = 11$ and (c) $N_c = 28$.

Fig. 27 shows contours of effective plastic strain in the matrix material for different values of macroscopic effective strain $\bar{\varepsilon} = 0, 0.033$ and 0.066 (identified with yellow markers in Figs. 25a and 25b). The results correspond to the three clustering microstructures investigated. Decreasing the number of clusters tends to increase the number of pores within each cluster (N_t is roughly the same, see Table 5), so that the pores are closer to each other (R_c is the same, see Table 5), which favors their interaction and early coalescence localization. Benson (1995) also showed that decreasing the radius of the clusters promotes coalescence in plane strain finite element simulations of specimens with clusters containing four cylindrical voids of the same size. Note that compared to the contour plots shown in Fig. 3 for the same microstructure but with randomly distributed pores, the plastic strain for the clustering microstructures is highly localized near the voids, giving rise to large values of plastic deformation in the intervoid ligaments of coalesced pores, while the plastic strain outside the clusters surroundings is much smaller. The clusters lead to increased heterogeneity in the plastic strain field of the unit-cell, and the less the number of clusters, the more localized the plastic deformation, as illustrated in the cut-views 27(c)-(f)-(i). The general trend is that, as the number of clusters decreases/increases, there are less/more localization bands connecting pores of different clusters.

Contours of effective plastic strain for the cluster indicated in 27(c) are included in Fig. 28 (the color coding is the same of Fig. 27). The cluster contains 27 voids which grow and rapidly interact with each other shortly after the loading starts, such that most of the pores are no longer spherical for $\bar{\varepsilon} = 0.033$, with the voids surrounding the largest pores displaying a mushroom shape with a flatten face corresponding to the formation of an intervoid ligament. The flattening of the voids generally starts earlier than in the case of the porous microstructures with randomly distributed voids (compare Figs. 4 and 28 and note that in the former the flattening starts at macroscopic strain of 0.066), since packing the voids into clusters decreases the distance between voids. For $\bar{\varepsilon} = 0.066$ the plastic strain in the surface of most pores is greater than 1, and the separation between voids is minimal, depicting the beginning of coalescence. The evolution of the cluster indicated in 27(f) for the microstructure $N_c = 11$ is included in Fig. 29. The cluster contains 16 voids, with a large pore which grows and flattens the surrounding voids, so that only the furthest pores maintain the spherical shape. The process of voids interaction and coalescence localization is the same described for the cluster in Fig. 28. The evolution of the cluster indicated in 27(i) for the microstructure $N_c = 28$ is included in Fig. 30. The cluster contains 5 pores, quite a few less than in the clusters shown in Figs. 28 and 29. The interaction between pores is apparent, yet, the change in shape of the pores seems to be less severe than for the clusters with more voids in which the neighboring pores are closer to each other. These calculations show the effect of clustering in the evolution of the shape and size of the pores.

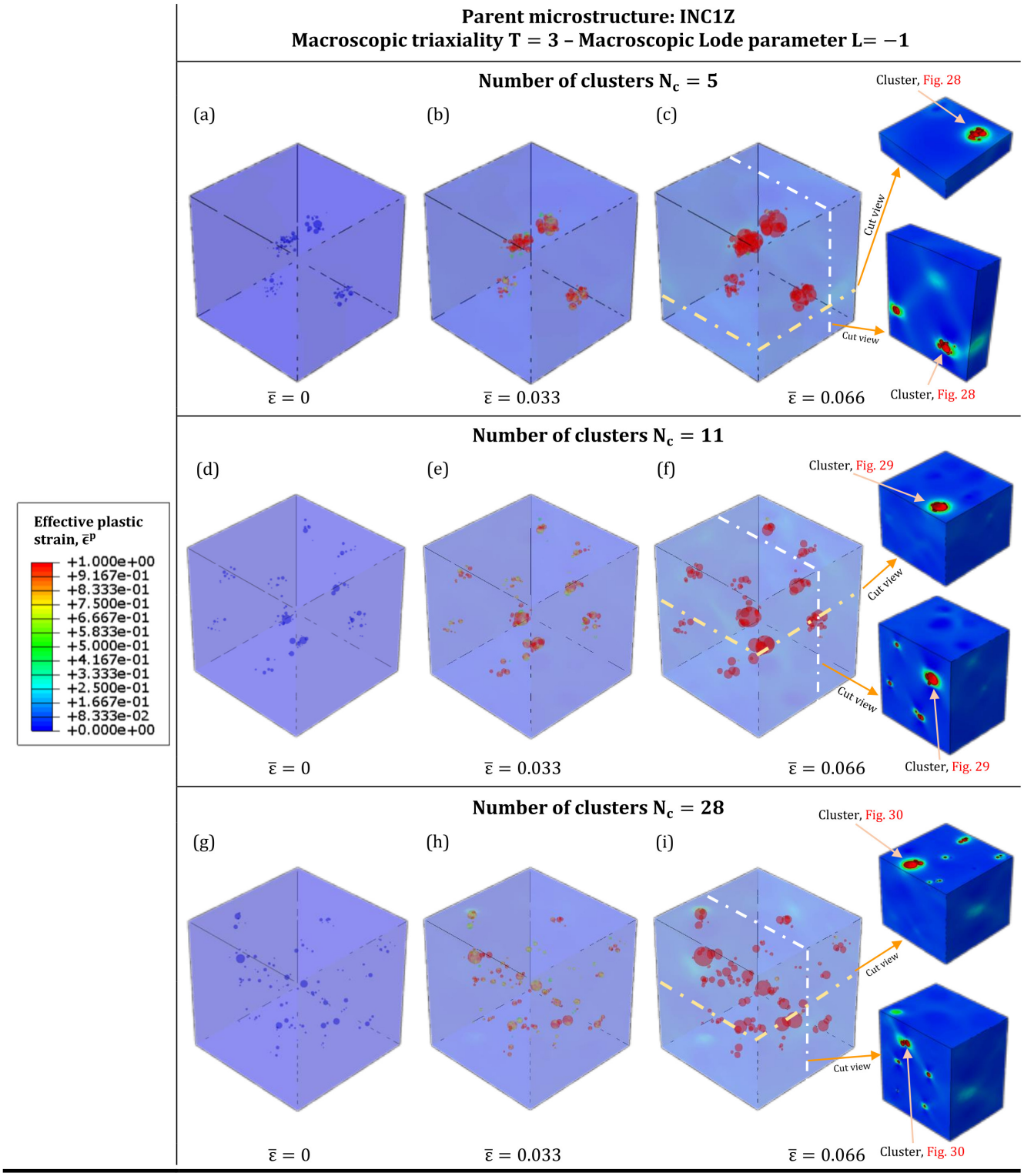

Figure 27: Results corresponding to parent porous microstructure INC1Z for stress triaxiality $T = 3$ and Lode parameter $L = -1$. Contours of effective plastic strain in the matrix material $\bar{\epsilon}^p$ for different values of macroscopic effective strain $\bar{\varepsilon} = 0, 0.033$ and 0.066. (a)-(c) Number of clusters $N_c = 5$. (d)-(f) Number of clusters $N_c = 11$. (g)-(i) Number of clusters $N_c = 28$. (For interpretation of the references to color in this figure legend, the reader is referred to the web version of this article.)

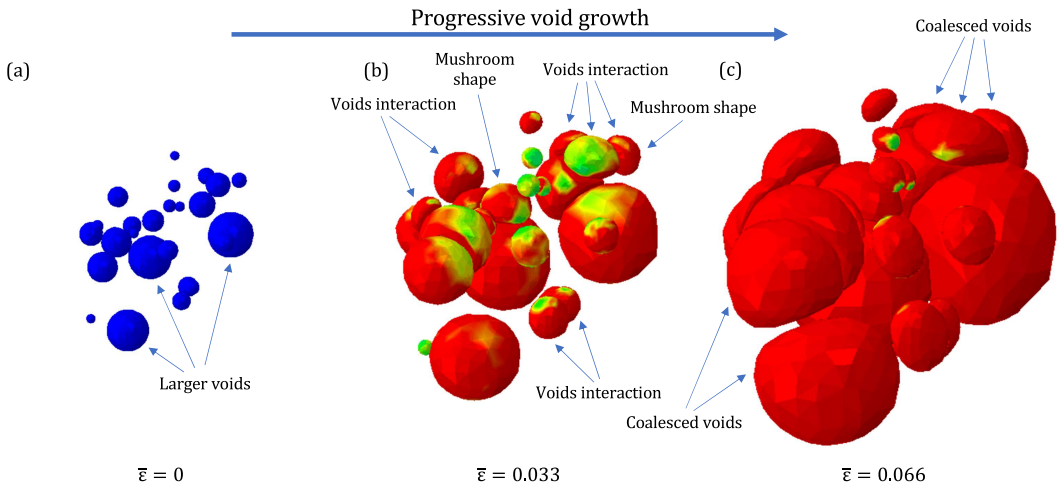

Figure 28: Results corresponding to parent porous microstructure INC1Z for number of clusters $N_c = 5$, stress triaxiality $T = 3$ and Lode parameter $L = -1$. Contours of effective plastic strain $\bar{\epsilon}^p$ for the cluster indicated in Fig. 27(c) for different values of macroscopic effective strain: (a) $\bar{\varepsilon} = 0$, (b) $\bar{\varepsilon} = 0.033$ and $\bar{\varepsilon} = 0.066$. The cluster contains 27 voids. (For interpretation of the references to color in this figure legend, the reader is referred to the web version of this article.)

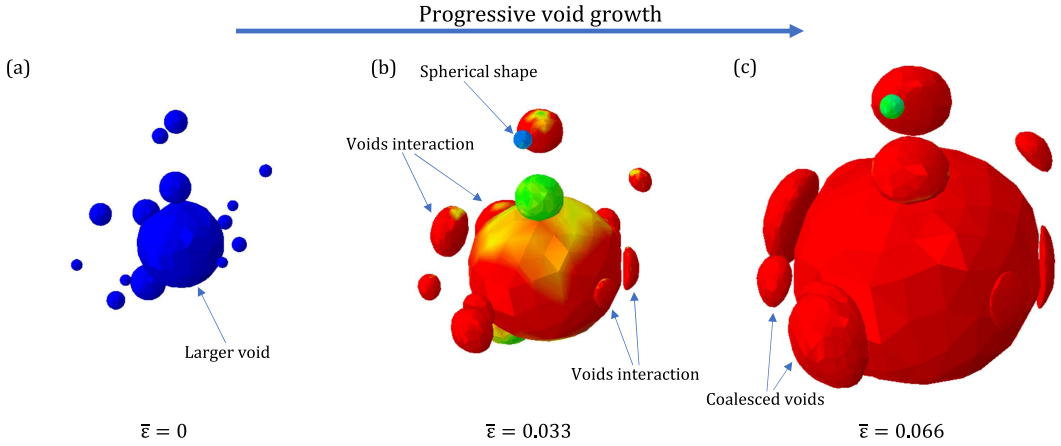

Figure 29: Results corresponding to parent porous microstructure INC1Z for number of clusters $N_c = 11$, stress triaxiality $T = 3$ and Lode parameter $L = -1$. Contours of effective plastic strain $\bar{\epsilon}^p$ for the cluster indicated in Fig. 27(f) for different values of macroscopic effective strain: (a) $\bar{\varepsilon} = 0$, (b) $\bar{\varepsilon} = 0.033$ and $\bar{\varepsilon} = 0.066$. The cluster contains 16 voids. (For interpretation of the references to color in this figure legend, the reader is referred to the web version of this article.)

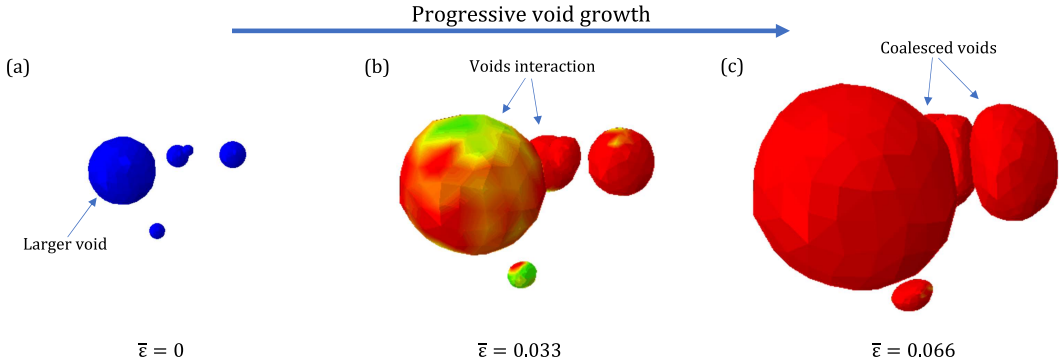

Figure 30: Results corresponding to parent porous microstructure INC1Z for number of clusters $N_c = 28$, stress triaxiality $T = 3$ and Lode parameter $L = -1$. Contours of effective plastic strain $\bar{\epsilon}^p$ for the cluster indicated in Fig. 27(i) for different values of macroscopic effective strain: (a) $\bar{\varepsilon} = 0$, (b) $\bar{\varepsilon} = 0.033$ and $\bar{\varepsilon} = 0.066$. The cluster contains 5 voids. (For interpretation of the references to color in this figure legend, the reader is referred to the web version of this article.)

7. Concluding remarks

In this paper, we have carried out finite element simulations of cubic unit-cells containing porous microstructures representative of three additively-manufactured metals –aluminium alloy AlSi10Mg (Al3XY), stainless steel 316L (SS5XY) and Inconel 718 (INC1Z)– and subjected to periodic boundary conditions for constant values of stress triaxiality $T = 1$, 2 and 3, and Lode parameter $L = -1$, 0 and 1. The main novelties of this research compared to recently published papers are: (1) considering a larger population of spherical voids to ensure that the numerical results are statistically significant and (2) including experimentally-measured distributions of void sizes. The initial void volume fraction of the porous microstructures investigated varies between 0.00564% and 1.75%, the number of the voids between 14 and 5715, and the diameter of the pores from 2.3 μm to 110 μm. Several realizations with different void sizes and positions have been generated for each of the porous microstructures considered. The simulations have been carried out with random spatial distributions of voids and with clusters of different sizes, and the results have been compared to unit-cells with a single central pore, and to calculations in which the material is modeled using Gurson plasticity. The main conclusions drawn from the analysis of the macroscopic effective response of the unit-cell, from the evolution of the void volume fraction, and from the growth of individual voids, are:

- Different realizations of the same porous microstructure lead to significant variations in the macroscopic effective stress and the void volume fraction evolution.
- Initial void volume fraction and distribution of void sizes play an important role on the effective mechanical properties of the porous aggregate and on the evolution of the porous microstructure.
- The interaction between neighboring pores make that voids of the same size grow at different speeds depending on their spatial location in the porous aggregate.
- For a given spatial and size distribution of voids, decreasing macroscopic triaxiality homogenizes the growth rate of the pores.
- For large macroscopic trixiality $T = 3$, the plastic deformation around the voids increases one order of magnitude faster than the macroscopic deformation of the porous aggregate.
- The voids volume evolution depends on the Lode parameter so that varying L from 0 to 1 leads more uniform growth rate of the pores.
- Varying the Lode parameter switches the collective behavior of the pores and the relative growth rate of individual voids.

- The growth of the pores makes them to interact and flatten, leading to the formation of a thin intervoid ligament subjected to large plastic strain which indicates coalescence localization.
- Microstructures with a large number of voids and increased void volume fraction favor fast strain softening and early coalescence localization.
- For a given voids size distribution, increasing the void volume fraction of multiple void microstructures slows down the normalized growth rate of pores.
- The agreement of Gurson model predictions with the calculations with actual porous microstructures depends on the initial void volume fraction and also on the distribution of void sizes.
- The differences between single pore and multiple pore calculations for the effective macroscopic stress and the void volume fraction increase with the macroscopic effective strain.
- As compared to the microstructures with random spatial distribution of voids, the clusters lead to increased heterogeneity in the plastic strain field of the porous aggregate.
- For a given voids size distribution and initial void volume fraction, decreasing the number of clusters promotes coalescence localization.
- The increase in the number of pores in the clusters causes the voids to interact and change shape, increasing the growth rate of the void volume fraction.

In summary, this work presents the most comprehensive study to date on the growth of voids in real porous microstructures, providing new insights into the effect that size and spatial distribution of voids have on the macroscopic response of the porous aggregate and the collective behavior of individual pores.

Funding

The research leading to these results has received funding from the European Research Council (ERC) under the European Union's Horizon 2020 research and innovation programme. Project PURPOSE, grant agreement 758056.

G. Vadillo acknowledges the financial support provided by the Spanish Ministry of Science and Innovation under the programme Proyectos I+D Excelencia 2017. Project APPLIED, DPI2017-88608-P.

Conflict of interest

The authors declare that they have no conflict of interest.

Author contributions

A. R. Vishnu: Conceptualization; Data curation; Formal analysis; Investigation; Software; Validation; Writing - original draft; Writing - review & editing. **G. Vadillo**: Conceptualization; Formal analysis; Funding acquisition; Investigation; Methodology; Software; Supervision; Writing - original draft; Writing - review & editing. **J. A. Rodríguez-Martínez**: Conceptualization; Formal analysis; Funding acquisition; Investigation; Methodology; Project administration; Resources; Supervision; Validation; Visualization; Writing - original draft; Writing - review & editing.

Appendix A. The effect of material behavior

The effect of the material behavior on the macroscopic effective response of the unit-cell, on the evolution of the normalized void volume fraction and on the growth of individual voids, is investigated for calculations performed with porous microstructure INC1Z and realization R1. The mechanical behavior of the material is modeled using the constitutive framework introduced in Section 2 and parameters corresponding to aluminum alloys 6111-T4 and 6013 (Kim et al., 2010; Ha et al., 2018), which show important differences in the initial yield stress and the strain hardening, see Table A.6 (in absence of experimental data, the strain rate sensitivity parameter for both materials is taken to be the same). The unit-cell simulations are performed with stress triaxiality $T = 3$ and Lode parameter $L = -1$.

Symbol	Property and units	Aluminium alloy 6111-T4	Aluminium alloy 6013
ρ_0	Initial density (kg/m^3)	2700	2700
G	Elastic shear modulus (GPa)	26.92	26.92
K	Bulk modulus (GPa)	58.33	58.33
σ_0	Initial yield stress parameter (MPa), Eq. (4)	503.7	556.06
n	Strain hardening exponent, Eq. (4)	0.233	0.201
m	Strain rate sensitivity exponent, Eq. (4)	0.01	0.01
ε_0	Reference strain, Eq. (4)	0	0.0062
$\dot{\varepsilon}_0$	Reference strain rate (s^{-1}), Eq. (4)	0.0001	0.0001

Table A.6: Numerical values of initial density, elastic constants and parameters of the yield stress corresponding to aluminum alloys 6111-T4 and 6013 (Kim et al., 2010; Ha et al., 2018).

Fig. A.31a includes the evolution of the macroscopic effective stress with the macroscopic effective strain $\bar{\varepsilon}$ for aluminum alloys 6111-T4 and 6013. The $\bar{\Sigma}/\sigma_0 - \bar{\varepsilon}$ curve corresponding to 6013 shows higher initial yield stress (see

Table A.6), yet, the strain softening process is faster and it starts at a lower value of the macroscopic effective strain (most likely because the strain hardening is smaller for aluminum alloy 6013, see Table A.6). The large difference in the strain softening of both materials is attributed to the faster increase of the void volume fraction for aluminum alloy 6013, see Fig. A.31b. These results make apparent that for a given initial microstructure, the material behavior has an important impact on the evolution of the porosity during loading.

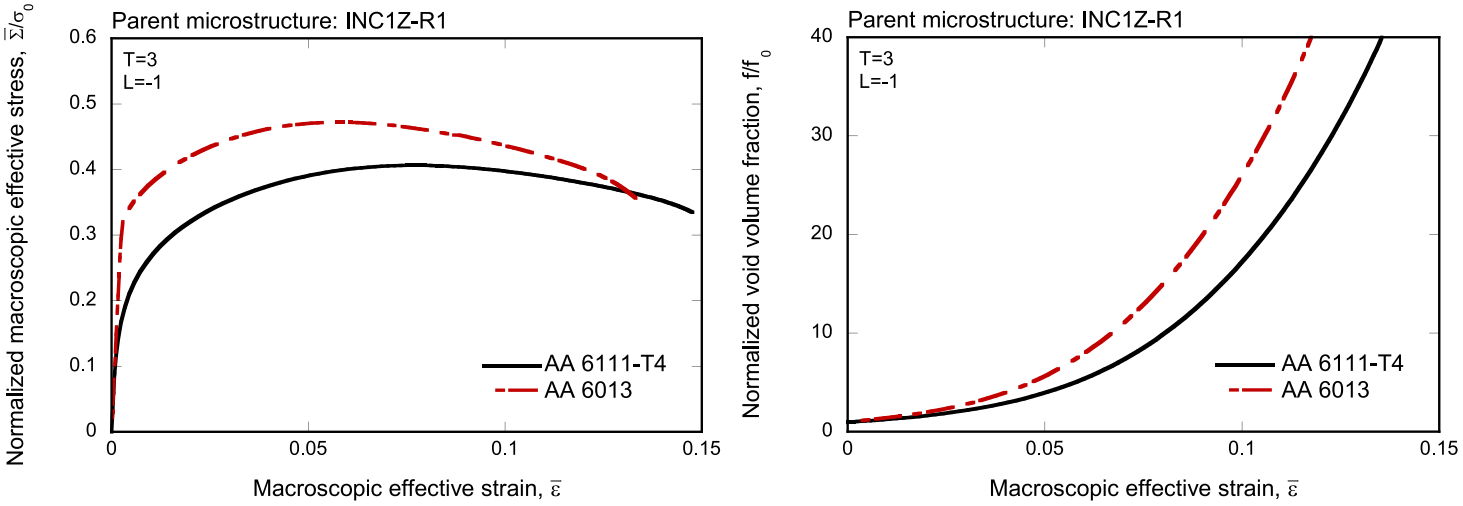

Figure A.31: Results corresponding to porous microstructure INC1Z and realization R1 for stress triaxiality $T = 3$ and Lode parameter $L = -1$. (a) Normalized macroscopic effective stress $\bar{\Sigma}/\sigma_0$ versus macroscopic effective strain $\bar{\varepsilon}$. (b) Normalized void volume fraction f/f_0 versus macroscopic effective strain $\bar{\varepsilon}$. Comparison of results obtained with material parameters corresponding to aluminum alloys 6111-T4 and 6013, see Table A.6.

Figs. A.32a and A.32b include the evolution of the volume of the five largest pores of the microstructure for aluminum alloys 6111-T4 and 6013, respectively. The results for both materials are qualitatively the same, i.e., the $V^{\text{void}}/V_0^{\text{void}} - \bar{\varepsilon}$ curves for the five pores have the same shape, and their relative order does not depend on the material. However, there are quantitative differences, as the volume of the pores corresponding to aluminum alloy 6013 increases faster, consistent with the results shown in Fig. A.31b.

The same trends and conclusions are obtained comparing the growth of the five smallest pores of the microstructure, see the results corresponding to aluminum alloys 6111-T4 and 6013 in Figs. A.33a and A.33b, respectively. The shape of the $V^{\text{void}}/V_0^{\text{void}} - \bar{\varepsilon}$ curves is very similar for the five voids considered, yet, the pores grow faster in the case of aluminum alloy 6013. These results suggest that the material parameters do not significantly alter the collective behavior of the voids during loading, yet, the mechanical response of the material seem to affect the rate of growth of the voids.

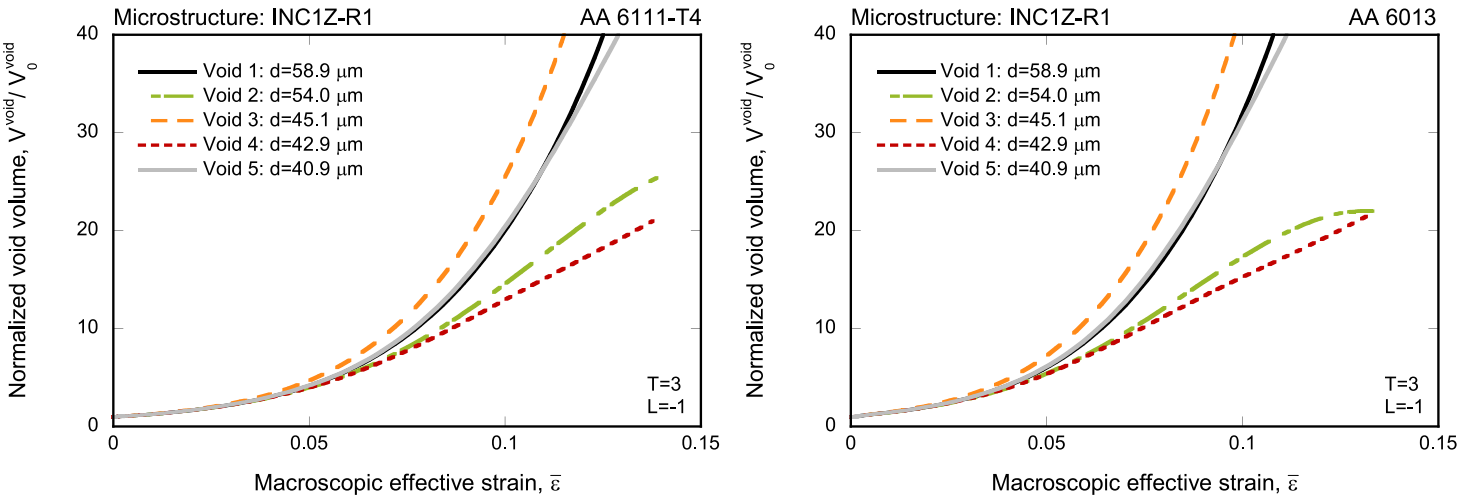

(a) (b)

Figure A.32: Results corresponding to porous microstructure INC1Z and realization R1 for stress triaxiality $T = 3$ and Lode parameter $L = -1$. Normalized void volume $V^{\text{void}}/V_0^{\text{void}}$ versus macroscopic effective strain $\bar{\varepsilon}$ for the largest pores of the microstructure with diameters varying from 58.9 μm to 40.9 μm. Two different material behaviors: (a) aluminum alloy 6111-T4 and (b) aluminum alloy 6013.

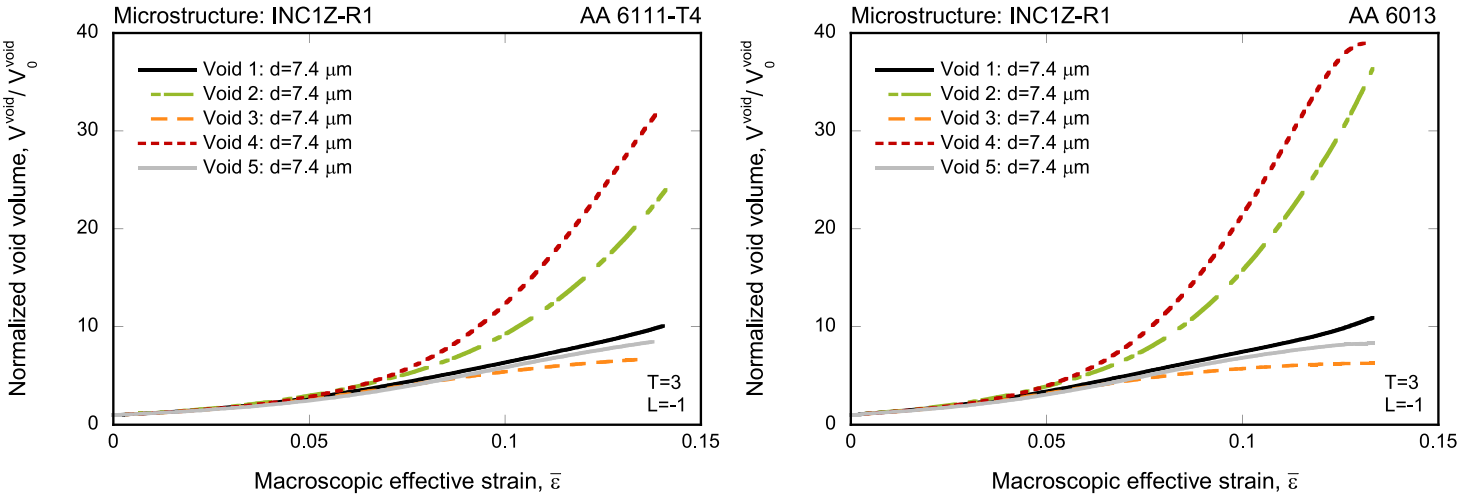

(a) (b)

Figure A.33: Results corresponding to porous microstructure INC1Z and realization R1 for stress triaxiality $T = 3$ and Lode parameter $L = -1$. Normalized void volume $V^{\text{void}}/V_0^{\text{void}}$ versus macroscopic effective strain $\bar{\varepsilon}$ for the smallest pores of the microstructure with diameter 7.4 μm. Two different material behaviors: (a) aluminum alloy 6111-T4 and (b) aluminum alloy 6013.

References

ABAQUS/Standard, 2019. Abaqus Standard v6.19 User's Manual. version 6.19 ed., ABAQUS Inc., Richmond, USA.

Barber, C.B., Dobkin, D.P., Huhdanpaa, H., 1996. The quickhull algorithm for convex hulls. ACM Transactions on Mathematical Software (TOMS) 22, 469–83.

Barlat, F., Aretz, H., Yoon, J.W., Karabin, M.E., Brem, J.C., Dick, R.E., 2005. Linear transfomation-based anisotropic yield functions. International Journal of Plasticity 21, 1009–39.

Benallal, A., Desmorat, R., Fournage, M., 2014. An assessment of the role of the third stress invariant in the Gurson approach for ductile fracture. European Journal of Mechanics A/Solids 47, 400–14.

Benson, D.J., 1995. The effects of void cluster size on ductile fracture. International Journal of Plasticity 11, 571–82.

Benzerga, A., Besson, J., 2001. Plastic potentials for anisotropic porous solids. European Journal of Mechanics A/Solids 20, 397–434.

Benzerga, A., Leblond, J., Needleman, A., Tvergaard, V., 2016. Ductile failure modeling. International Journal of Fracture 201, 29–80.

Benzerga, A.A., Besson, J., Pineau, A., 2004. Anisotropic ductile fracture: Part II: Theory. Acta Materialia 52, 4639–50.

Benzerga, A.A., Leblond, J.B., 2010a. Ductile fracture by void growth and coalescence. Advances in Applied Mechanics 44, 169–305.

Benzerga, A.A., Leblond, J.B., 2010b. Ductile fracture by void growth to coalescence. Advances in applied mechanics 44, 169–305.

Cadet, C., Besson, J., Flouriot, S., Forest, S., Kerfriden, P., Lacourt, L., de Rancourt, V., 2022. Strain localization analysis in materials containing randomly distributed voids: Competition between extension and shear failure modes. Journal of the Mechanics and Physics of Solids 166, 104933.

Cadet, C., Besson, J., Flouriot, S., Forest, S., Kerfriden, P., de Rancourt, V., 2021. Ductile fracture of materials with randomly distributed voids. International Journal of Fracture 230, 193–223.

Chen, Z., Dong, X., 2009. The GTN damage model based on Hill'48 anisotropic yield criterion and its application in sheet metal forming. Computational Materials Science 44, 1013–21.

Cheng, L., Guo, T.F., 2007. Void interaction and coalescence in polymeric materials. International Journal of Solids and Structures 44, 1787–808.

Chu, C.C., Needleman, A., 1980. Void nucleation effects in biaxially stretched sheets. Journal of Engineering Materials and Technology 102, 249–56.

Cox, T., Low, J.R., 1974. An investigation of the plastic fracture of AISI 4340 and 18 Nickel-200 grade maraging steels. Metallurgical and Materials Transactions B 5, 1457–70.

Cvitanić, V., Vlak, F., Lozina, Ž., 2008. A finite element formulation based on non-associated plasticity for sheet metal forming. International Journal of Plasticity 24, 646–87.

Dæhli, L.E.B., Morin, D., Børvik, T., Hopperstad, O.S., 2018. A Lode-dependent Gurson model motivated by unit cell analyses. Engineering Fracture Mechanics 190, 299–318.

Dakshinamurthy, M., Kowalczyk-Gajewska, K., Vadillo, G., 2021. Influence of crystallographic orientation on the void growth at the grain boundaries in bi-crystals. International Journal of Solids and Structures 212, 61–79.

Danas, K., Aravas, N., 2012. Numerical modeling of elasto-plastic porous materials with void shape effects at finite deformations. Composites Part B: Engineering 43, 2544–59.

Danas, K., Ponte-Castañeda, P., 2009. A finite-strain model for anisotropic viscoplastic porous media: I–Theory. European Journal of Mechanics-A/Solids 28, 387–401.

Danas, K., Ponte-Castañeda, P., 2012. Influence of the Lode parameter and the stress triaxiality on the failure of elasto-plastic porous materials. International Journal of Solids and Structures 49, 1325–42.

Duva, J.M., 1986. A constitutive description of nonlinear materials containing voids. Mechanics of Materials 5, 317–29.

Faleskog, J., Gao, X., Shih, C., 2000. Cell model for nonlinear fracture analysis - I. Micromechanics calibration. Journal of the Mechanics and Physics of Solids 89, 355–73.

Gologanu, M., Leblond, J.B., Perrin, G., Devaux, J., 1997. Recent extensions of Gurson's model for porous ductile metals. P. Suquet (Ed.), Continuum Micromechanics, Springer-Verlag, New York , 61–130.

Graham-Brady, L., 2010. Statistical characterization of meso-scale uniaxial compressive strength in brittle materials with randomly occurring flaws. International Journal of Solids and Structures 47, 2398–413.

695 Gărăjeu, M., Michel, J.C., Suquet, P., 2000. A micromechanical approach of damage in viscoplastic materials by evolution
696 in size, shape and distribution of voids. Computer Methods in Applied Mechanics and Engineering 183, 223–46.

697 Guo, Z.Y., Caner, F., Peng, X.Q., Moran, B., 2008. On constitutive modelling of porous neo-hookean composites.
698 International Journal of Solids and Structures 56, 2338–57.

699 Gurson, A.L., 1975. Plastic flow and fracture behavior of ductile materials, incorporating void nucleation, growth, and
700 interaction. Ph.D. thesis. Brown University Providence, RI.

701 Gurson, A.L., 1977. Continuum theory of ductile rupture by void nucleation and growth. Part I: Yield criteria and flow
702 rules for porous ductile media. ASME Journal of Engineering Materials and Technology 99, 2–15.

703 Ha, J., Baral, M., Korkolis, Y.P., 2018. Plastic anisotropy and ductile fracture of bake-hardened AA6013 aluminum
704 sheet. International Journal of Solids and Structures 155, 123–39.

705 Hancock, J.W., Mackenzie, A.C., 1976. On the mechanisms of ductile failure in high-strength steels subjected to multi-
706 axial stress-states. Journal of the Mechanics and Physics of Solids 24, 147–69.

707 Hannard, F., Castin, S., Maire, E., Mokso, R., Pardoen, T., Simar, A., 2017. Ductilization of aluminium alloy 6056 by
708 friction stir processing. Acta Materialia 130, 121–36.

709 Hosseini, N., Nieto-Fuentes, J.C., Dakshinamurthy, M., Rodríguez-Martínez, J.A., Vadillo, G., 2022. The effect of
710 material orientation on void growth. International Journal of Plasticity 148, 103149.

711 Hure, J., 2021. Yield criterion and finite strain behavior of random porous isotropic materials. European Journal of
712 Mechanics A/Solids 85.

713 Jackiewicz, J., 2011. Use of a modified Gurson model approach for the simulation of ductile fracture by growth and
714 coalescence of microvoids under low, medium and high stress triaxiality loadings. Engineering Fracture Mechanics 78,
715 487–502.

716 Keralavarma, S.M., Benzerga, A.A., 2010. A constitutive model for plastically anisotropic solids with non-spherical
717 voids. Journal of the Mechanics and Physics of Solids 58, 874–901.

718 Khan, I., Bhasin, V., 2017. On the role of secondary voids and their distribution in the mechanism of void growth and
719 coalescence in porous plastic solids. International Journal of Solids and Structures 108, 203–15.

720 Kim, D., Lee, W., Kim, J., Kim, C., Chung, K., 2010. Formability evaluation of friction stir welded 6111-T4 sheet with
721 respect to joining material direction. International Journal of Mechanical Sciences 52, 612–25.

722 Kim, J., Gao, X., Srivatsan, T.S., 2004a. Modeling of void growth in ductile solids: effects of stress triaxiality and initial
723 porosity. Engineering Fracture Mechanics 71, 379–400.

724 Kim, J., Gao, X., Srivatsan, T.S., 2004b. Modeling of void growth in ductile solids: effects of stress triaxiality and initial
725 porosity. Engineering Fracture Mechanics 71, 379–400.

726 Kim, J., Zhang, G., Gao, X., 2007. Modeling of ductile fracture: Application of the mechanism-based concepts. Inter-
727 national Journal of Solids and Structures 44, 1844–62.

728 Kristoffersen, M., Costas, M., Koenis, T., Brøtan, V., Paulsen, C.O., Børvik, T., 2020. On the ballistic perforation
729 resistance of additive manufactured AlSi10Mg aluminium plates. International Journal of Impact Engineering 137,
730 103476.

731 Leblond, J.B., Morin, L., 2014. Gurson's criterion and its derivation revisited. Journal of Applied Mechanics 81(5),
732 051012.

733 Leblond, J.B., Perrin, G., Devaux, J., 1995. An improved Gurson-type model for hardenable ductile metals. European
734 Journal of Mechanics A/Solids 14, 499–527.

735 Maire, E., Withers, P., 2014. Quantitative X-ray tomography. International Materials Reviews 59, 1–43.

736 Marvi-Mashhadi, M., Vaz-Romero, A., Sket, F., Rodríguez-Martínez, J.A., 2021. Finite element analysis to determine
737 the role of porosity in dynamic localization and fragmentation: Application to porous microstructures obtained from
738 additively manufactured materials. International Journal of Plasticity 143, 102999.

739 McClintock, F., 1968. A criterion for ductile fracture by the growth of holes. Journal of Applied Mechanics 35, 363–71.

740 McVeigh, C., Vernerey, F., Liu, W.K., Moran, B., Olson, G., 2007. An interactive micro-void shear localization mechanism
741 in high strength steels. Journal of the Mechanics and Physics of Solids 55, 225–44.

742 Mises, R.V., 1928. Mechanik der plastischen formänderung von kristallen. ZAMM - Journal of Applied Mathematics
743 and Mechanics / Zeitschrift für Angewandte Mathematik und Mechanik 8, 161–85.

744 Monchiet, V., Bonnet, G., 2013. A Gurson-type model accounting fot void size effects. International Journal of Solids
745 and Structures 50, 320–7.

Nahshon, K., Hutchinson, J.W., 2008. Modification of the Gurson model for shear failure. European Journal of Mechanics A-Solid 27, 1–17.

Needleman, A., 1972. Void growth in an elastic-plastic medium. Journal of Applied Mechanics 39, 964–70.

Nieto-Fuentes, J.C., Espinoza, J., Sket, F., Rodríguez-Martínez, J.A., 2022a. High-velocity impact fragmentation of additively-manufactured metallic tubes. Submitted for Publication doi:10.31224/2627.

Nieto-Fuentes, J.C., Jacques, N., Marvi-Mashhadi, M., N'souglo, K.E., Rodríguez-Martínez, J.A., 2022b. Modeling dynamic formability of porous ductile sheets subjected to biaxial stretching: Actual porosity versus homogenized porosity. International Journal of Plasticity 158, 103418.

Pardoen, T., Hutchinson, J.W., 2003. Micromechanics-based model for trends in toughness of ductile metals. Acta Materialia 51, 133–48.

Pineau, A., Benzerga, A.A., Pardoen, T., 2016. Failure of metals I: Brittle and ductile fracture. Acta Materialia 107, 424–83.

Reboul, J., Srivastava, A., Osovski, S., Vadillo, G., 2020. Influence of strain rate sensitivity on localization and void coalescence. International Journal of Plasticity 125, 265–79.

Rice, J.R., Tracey, D.M., 1969. On the ductile enlargement of voids in triaxial stress fields. Journal of the Mechanics and Physics of Solids 17, 201–17.

Shakoor, M., Bernacki, M., Bouchard, P.O., 2018. Ductile fracture of a metal matrix composite studied using 3D numerical modeling of void nucleation and coalescence. Engineering Fracture Mechanics 189, 110–32.

Tekoğlu, C., Hutchinson, J.W., Pardoen, T., 2015. On localization and void coalescence as a precursor to ductile fracture. Philosophical Transactions of the Royal Society A: Mathematical, Physical and Engineering Sciences 373, 20140121.

Tekoğlu, C., Koçhan, B., 2022. Unit cell calculations under fully characterized stress states. International Journal of Plasticity 156, 103358.

Tekoğlu, C., Leblond, J.B., Pardoen, T., 2012. A criterion for the onset of void coalescence under combined tension and shear. Journal of the Mechanics and Physics of Solids 60, 1363–81.

Thomason, P., 1985. A three-dimensional model for ductile fracture by the growth and coalescence of microvoids. Acta Metallurgica 33 (6), 1087–95.

772 Thomason, P.F., 1990. Ductile fracture of metals.

773 Thomson, C., Worswick, M., Pilkey, A., Lloyd, D., 1998. Modeling void nucleation and growth within periodic clusters
774 of particles. Journal of the Mechanics and Physics of Solids 47, 1–26.

775 Thomson, C.I.A., Worswick, M.J., Pilkey, A.K., Lloyd, D.J., 2003. Void coalescence within periodic clusters of particles.
776 Journal of the Mechanics and Physics of Solids 51, 127–46.

777 Thoré, P., Pastor, F., Pastor, J., D., K., 2009. Closed-form solutions for the hollow sphere model with coulomb and
778 drucker prager materials under isotropic loadings. Comptes-Rendus Mécanique 337, 260–7.

779 Trejo Navas, V.M., Bernacki, M., Bouchard, P.O., 2018. Void growth and coalescence in a three-dimensional non-periodic
780 void cluster. International Journal of Solids and Structures 139-140, 65–78.

781 Tvergaard, V., 1981. Influence of voids on shear band instabilities under plane strain conditions. International Journal
782 of Fracture 17, 389–407.

783 Tvergaard, V., 2016. Effect of void cluster on ductile failure evolution. Meccanica 51, 3097–105.

784 Tvergaard, V., 2017. Nucleation from a cluster of inclusions, leading to void coalescense. International Journal of
785 Mechanical Sciences 133, 631–8.

786 Tvergaard, V., Needleman, A., 1984. Analysis of the cup-cone fracture in a round tensile bar. Acta Metallurgica 32,
787 157–69.

788 Vadillo, G., Reboul, J., Fernández-Sáez, J., 2016. A modified gurson model to account for the influence of the Lode
789 parameter at high triaxialities. European Journal of Mechanics-A/Solids 56, 31–44.

790 Vishnu, A.R., Marvi-Mashhadi, M., Nieto-Fuentes, J.C., Rodríguez-Martínez, J.A., 2022a. New insights into the role of
791 porous microstructure on dynamic shear localization. International Journal of Plasticity 148, 103150.

792 Vishnu, A.R., Nieto-Fuentes, J.C., Rodríguez-Martínez, J.A., 2022b. Shear band formation in porous thin-walled tubes
793 subjected to dynamic torsion. International Journal of Solids and Structures 252, 111837.

794 Wen, J., Huang, Y., Hwang, K., Kiu, C., Li, M., 2005. The modified Gurson model accounting for the void size effect.
795 International Journal of Plasticity 21, 381–95.

796 Xue, L., 2008. Constitutive modeling of void shearing effect in ductile fracture of porous materials. Engineering Fracture
797 Mechanics 75, 3343–66.

798 Yoon, J.W., Barlat, F., Dick, R.E., Karabin, M.E., 2006. Prediction of six or eight ears in a drawn cup based on a new
799 anisotropic yield function. International Journal of Plasticity 22, 174–93.